VISER
www.viserdata.com

RESEARCH AND APPLICATION OF MATERIALS SCIENCE

ISSN:2661-4464(online) 2661-4456(print)
Volume 5 No. 2 2023

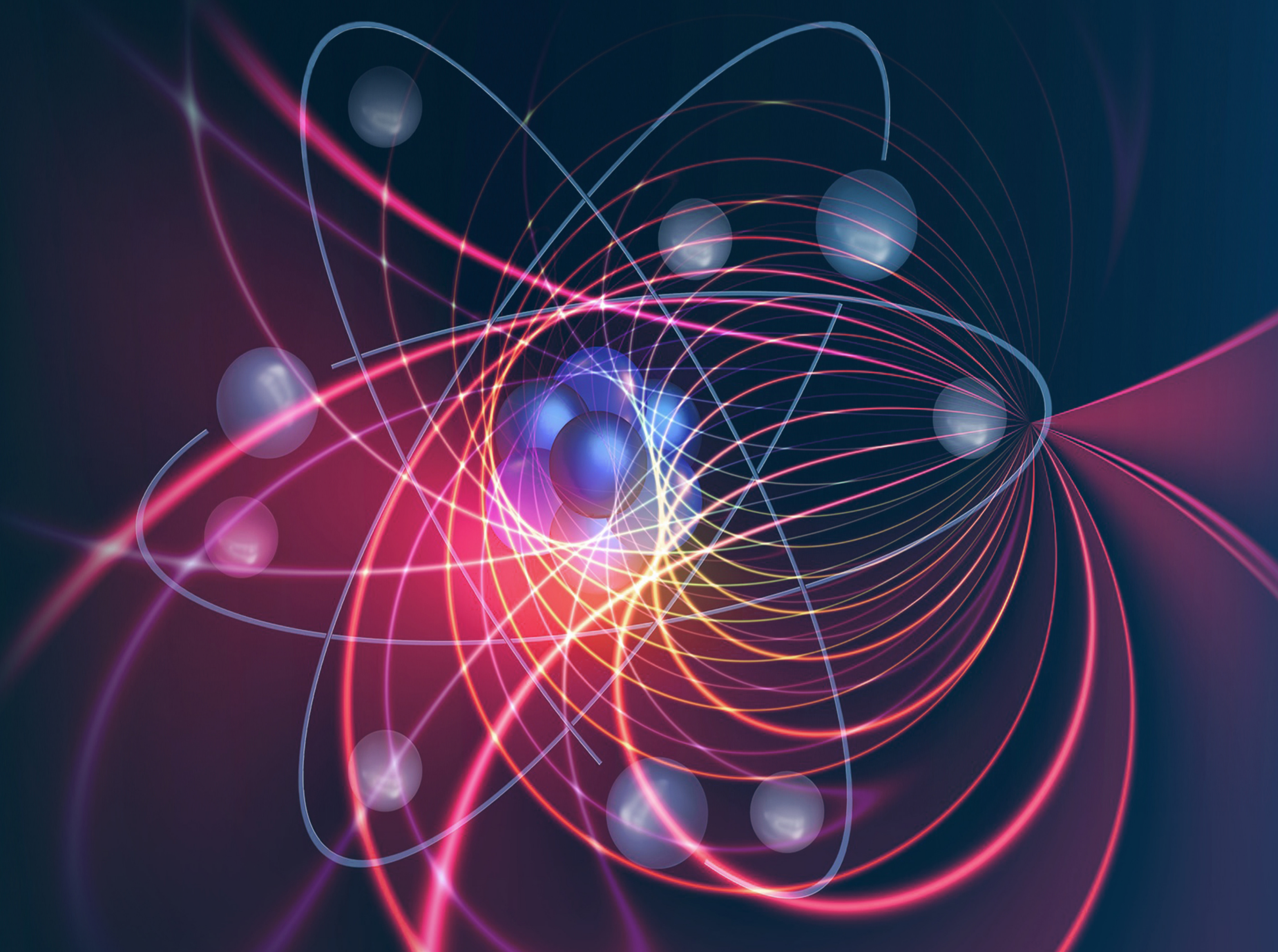

COMPANY INTRODUCTION

Viser Technology Pte. Ltd. was founded in Singapore with branch offices in both Hebei and Chongqing, China. Viser focuses on publishing scientific and technological journals and books that promote the exchange of scientific and technological findings among the research community and around the globe. Despite being a young company, Viser is actively connecting with well-known universities, research institutes, and indexation database, and has already established a stable collaborative relationship with them. We also have a group of experienced editors and publishing experts who are dedicated to publishing high-quality journal and book contents. We offer the scholars various academic journals covering a variety of subjects and we are committed to reducing the hassles of scholarly publishing. To achieve this goal, we provide scholars with an all-in-one platform that offers solutions to every publishing process that a scholar needs to go through in order to show their latest finding to the world.

Research and Application of Materials Science

Publisher: Viser Technology Pte. Ltd.
ISSN: 2661-4464(online)
2661-4456(print)
Frequency: Semi-annual
Add.:21 Woodlands Close, #08-18
Primz Bizhub SINGAPORE (737854)
https://www.viserdata.com/

Editors:
Yajun Lian
Yanli Liu
John Wilson
Nike Yough
Mart Chen
Qiuyue Su
Debra Hamilton
Xin Di
Jennifer M Dohy
Xiuli Li
Edward Adam Davis
Liangjun Qiu
Designer: Anson Chee

Research and Application of Materials Science

Volume 5 No.2 (2023)

CONTENTS

Viser Technology Pte. Ltd.
Research and Application of Materials Science
DOI: 10.33142/rams.v5i2.12704

Research Article **Open Access**

Improved Corrosion Behavior of Biodegradable Mg-4Zn-1Mn Alloy Modified by Sr/F co-doped CaP Micro-arc Oxidation Coatings

Weirong LI[1*], Yanfang LI [1], Qian LI [1], Xuan XIONG[1], Fangfei LIU[1], Ronghui LI [1], Heng LI[1], Dong PANG[1], Jia LU[2], Xuan ZHANG [2*]

1. Dongguan Eontec Co., Ltd., Dongguan, Guangdong, 523000, China
2. School of Mechanical Engineering, Tiangong University, Tianjin 300387, China

[*] ***Corresponding Author:*** *Weirong LI, Xuan ZHANG, E-mail: liwr@e-ande.com; zhangxuan199706@163.com*

Abstract

The Sr/F co-doped CaP (Sr/F-CaP) coatings were prepared by micro-arc oxidation (MAO) under different voltages to modify the microstructure and corrosion behavior of Mg-4Zn-1Mn alloy. The surface and interface characteristics investigated using scanning electron microscopy (SEM) and energy dispersive X-ray spectrometer (EDS) showed that the MAO coatings displayed uneven crater-like holes and tiny cracks under lower voltage, while they exhibited relatively homogeneous crater-like holes without cracks under higher voltage. The thickness of MAO coatings increased with increasing voltage. The corrosion behavior of Mg-4Zn-1Mn alloy was improved by the MAO coatings. The MAO coatings prepared under 450 V and 500 V voltages possessed the best corrosion resistance with regard to the electrochemical corrosion tests and immersion corrosion tests, respectively. The MAO coatings fabricated under 450-500 V could provide a better corrosion protection effect for the substrate.

Keywords: *Biodegradable Mg alloys; Mg-4Zn-1Mn alloy; Micro-arc oxidation; Sr/F co-doped CaP coatings*

1 Introduction

As a representative kind of biodegradable metals, Mg alloys have recently attracted great research interest as temporary implants in the orthopedic and cardiovascular fields [1-2]. Compared with traditional biomedical metals (stainless steels, Ti alloys, NiTi alloys and Co-Cr alloys, etc.), Mg alloys exhibit the following advantages[3-5]: Firstly, they have lower density, higher specific strength and closer Young's modulus to that of human bone; Secondly, they can be gradually dissolved in physiological environment after tissue repairing to avoid a secondary removal surgery; Thirdly, their corrosion products of Mg oxides/hydroxides are nontoxic and may even promote cell viability. However, the insufficient mechanical support and excess hydrogen accumulation caused by the rapid corrosion of Mg alloys usually hinder the tissue repairing process in early implantation period, which is the main obstacle for their clinical applications [6-7]. Therefore, enhancing the corrosion resistance of Mg alloys is the key means to solve their clinical problems.

Surface modification via proper technologies such as ion implantation, magnetron sputtering, anodic oxidation, electrochemical deposition, sol-gel and spin coating has been evidenced to be an effective method to improve the corrosion behavior of Mg alloys [8-13]. Among them, the micro-arc oxidation (MAO) is a very promising surface modification method for Mg alloys, which can regulate their corrosion behavior by preparing corrosion-resistant ceramic coatings with desired microstructure, morphology and chemical composition [14-17]. Generally, the MAO coatings exhibit a bilayer feature: the outer layer with porous microstructure contributes to promote the adhesion, migration and growth of cells; the inner layer with dense microstructure helps to enhance the corrosion resistance of outer layer and increase its bonding strength with the substrate [18]. The major factors influencing MAO coatings are electrolyte composition and electrical parameters including working mode, voltage, current density, oxidation time, frequency, duty ratio, etc. Ly et al. compared the effect of different working modes (unipolar, bipolar, unipolar followed by bipolar) on the corrosion resistance of MAO coatings on the Mg-4.71Zn-0.6Ca alloy surface, and found that the

Received on September 22, 2023; Accepted on November 2, 2023

MAO coating prepared under hybrid mode had better anti-corrosion ability than the other two modes[19]. Lin et al. fabricated the forsterite-containing MAO coatings on the surface of ZK60 Mg alloy via a silicate electrolyte-based MAO treatment under different voltages, and the results showed that the corrosion resistance of MAO coatings were increased with increasing voltage [20]. Zhu et al. further enhanced the corrosion resistance of molybdate conversion coating on the surface of AZ91D Mg alloy after a MAO treatment in the electrolyte with Na_2SiO_3 as main salt, and observed that the ceramic coating was gradually formed as the oxidation time was prolonged [21].

Considering that Ca and P elements are the main components of human bone, the CaP MAO coatings have been prepared to simultaneously improve the corrosion behavior and biocompatibility of Mg alloys [22-23]. However, the single CaP coatings lack adequate bioactivity like antibacterial and osteogenic properties, which can be compensated by doping some functional elements. As a necessary trace element for human body, Sr element can not only stimulate bone formation but also inhibit bacterial growth, which is an ideal element for bone regeneration [24]. As a participating element for multifarious metabolic activities, F element can facilitate osteoblasts differentiation to accelerate bone formation and provide broad-spectrum antibacterial property[25]. Therefore, the co-doping of Sr and F elements into the CaP coatings (Sr/F-CaP coatings) is expected to have satisfactory corrosion resistance and higher bioactivity with both antibacterial and osteogenic properties. To our knowledge, there are no systematic researches on the biodegradable Mg alloys modified by the Sr/F-CaP coatings. In this work, the effects of Sr/F-CaP coatings prepared by MAO under different voltages on the microstructure and corrosion behavior of extruded Mg-4Zn-1Mn alloy were investigated.

2 Experimental Procedures

2.1 Sample preparation

2.1.1 Substrate

The high-purity Mg (＞99.99%), high-purity Zn (＞99.99%) and Mg-5Mn intermediate alloy were used as the raw materials. The raw materials were melted using an electric resistance furnace protected by the mixed gas of 0.3 vol.% SF_6, 50 vol.% CO_2 and 49.7 vol.% air. The alloy melt was purged at 760 ℃ for 10 min, held at 720 ℃ for 15 min, poured into a mild steel crucible preheated at 700 ℃ and cooled at room temperature to get the Mg-4Zn-1Mn ingot (Φ100 mm×200 mm). After that, the ingot was machined to remove the oxides and impurities on the surface to get the initial rod with a diameter of 80 mm. For extrusion process, the initial rod was preheated at 450 ℃ and extruded at 380 ℃ with an extrusion rate of 1.5 mm/min and an extrusion ratio of 64 to obtain the Mg-4Zn-1Mn rod (Φ10 mm×1000 mm). Before MAO treatment, the rod was cut into Φ10 mm×3 mm sheets by the electro-discharge machining. The sheets (used as the substrates) were mechanically polished, ultrasonically cleaned with distilled water and dried in air.

2.1.2 MAO coatings

The MAO coatings were fabricated using a home-made MAO power supply under a constant voltage control mode. The samples and a stainless-steel plate with a size of 200 mm×200 mm×1 mm were served as the anode and the cathode, respectively. The electrolyte was composed of 15 g/L $Ca(H_2PO_4)_2\cdot H_2O$, 15 g/L $Na_3PO_4\cdot 12H_2O$, 1.5 g/L CaF_2 and 2 g/L $Sr(OH)_2\cdot 8H_2O$. The electrolyte temperature was kept at 20-25 ℃ by a circulating water-cooling system. The samples and corresponding MAO processing parameters are listed in Table 1. After MAO process, the samples were rinsed with distilled water and dried in air.

Table 1 The samples and corresponding MAO processing parameters

Samples	Voltage (V)	Frequency (Hz)	Duty cycle (%)	Oxidation time (min)
Sr/F-CaP-400	400	600	30	8
Sr/F-CaP-450	450	600	30	8
Sr/F-CaP-500	500	600	30	8

2.2 Microstructure characterization

The surface and cross-sectional morphologies of the MAO coatings were analyzed by a scanning electron microscopy (SEM, Quanta-450, FEI, USA) and an energy dispersive X-ray spectrometer (EDS, Oxford Instruments, UK). The phase constitutions of the MAO coatings were identified by an X-ray diffractometer (XRD, D8 Advance, Bruker, Germany) with a Cu K_α radiation at a scanning rate of 4^{o}/min in the 2θ range of 10^{o}～85^{o}.

2.3 Corrosion behavior evaluation

2.3.1 Electrochemical corrosion tests

The electrochemical corrosion behavior of the samples before and after MAO treatment was studied at an electrochemical workstation (CHI660e, CH Instruments Inc., China). A typical three-electrode system was employed with the samples as the working electrode, a platinum electrode as the counter electrode and a saturated calomel electrode (SCE) as the reference electrode. The measurements were performed in the simulated body fluid (SBF) at $37\pm1\ ^{o}$C. The composition of the SBF included 8.035 g/L NaCl, 0.355 g/L $NaHCO_3$, 0.225 g/L KCl, 0.231 g/L $KH_2PO_4\cdot 3H_2O$, 0.311 g/L $MgCl_2\cdot 6H_2O$, 39 mL HCl (1.0M), 0.292 g/L $CaCl_2$, 0.072 g/L Na_2SO_4 and 6.118 g/L Tris[26]. The electrochemical corrosion tests of open circuit potential (OCP), impedance spectroscopy (EIS) and potentiodynamic polarization (PDP) were conducted in sequence. The OCP values were recorded for 30 min to realize surface stabilization. The EIS results were measured with an AC amplitude perturbing signal of 5 mV and a scan frequency from 100 kHz to 10 mHz. The EIS data were fitted by the ZSimpWin software. The PDP curves were tested at a scan rate of 1 mV/s with a potential range from -2 V/SCE to -1 V/SCE. The PDP data were fitted by the CHI660e software.

2.3.2 Immersion corrosion tests

The immersion corrosion behavior of the samples before and after MAO treatment was investigated in the SBF at 37 ±1 °C according to the ASTM-G31-72 standard. After different immersion times (2, 6 and 14 days), the samples were taken out, rinsed with distilled water and dried in air. The morphology and composition of the corrosion products at specific immersion time were analyzed by the SEM and EDS. The pH value of SBF during immersion corrosion tests was monitored by a pH meter (PHB-4, INESA Scientific Instrument, Shanghai, China). The weight loss of the samples was measured by a scale (0.01 mg in accuracy) after removing the corrosion products with the chromic acid solution (200 g/L CrO_3 and 10 g/L $AgNO_3$).

3 Results and Discussion

3.1 Microstructure

Figure 1 shows the surface and the cross-section morphologies of the samples. The substrate surface is relatively smooth and flat, which is convenient for the subsequent coating process (Figure 1a). The Sr/F-CaP-400 sample surface is characterized by uneven crater-like holes and tiny cracks, whose average thickness of its MAO coating is about 7.8 μm (Figure 1b and 1e). There appears a transverse crack in the MAO coating of the Sr/F-CaP-400 sample, which may be caused by relatively low voltage of 400 V under a short oxidation time of 8 min. The growth rate of MAO coating is too small to prepare a thick-enough and high-quality coating under low voltage, which leads to the formation of a crack perpendicular to the growth direction. This can be evidenced by its unfavorable surface morphology and smallest average thickness, as shown in Figure 1b and 1e. The Sr/F-CaP-450 sample surface exhibits a compact morphology with homogeneous crater-like holes and its MAO coating has an average thickness of 9.2 μm (Figure 1c and 1f). The Sr/F-CaP-500 sample surface is featured with a dense morphology with various crater-like holes and its MAO coating has an average thickness of 11.0 μm (Figure 1d and 1g). The porous structure on the surface is generated due to the sparks discharge effect occurs in the MAO process, which could facilitate the cell growth in some degree [27]. The bonding interface between substrate and MAO coating becomes tighter as the voltage increases. With increasing voltage, the MAO coating shows a slightly larger thickness with relatively uniform porous structure and inconspicuous cracks. Similar phenomenon can also be found in the reference[28].

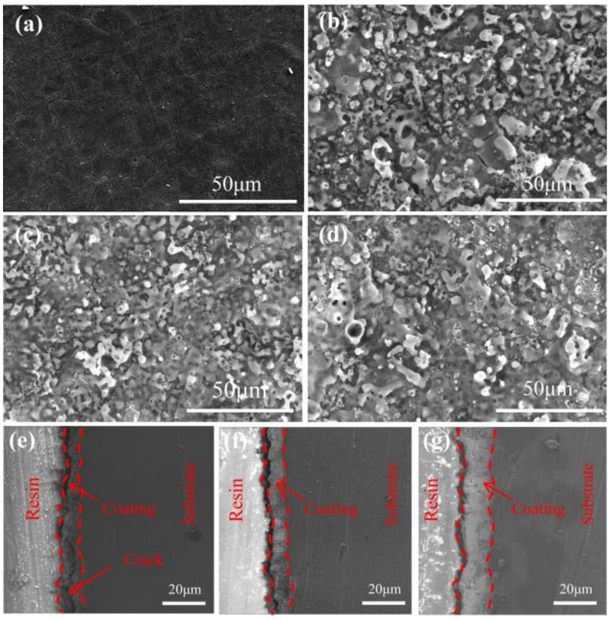

Figure 1 (a-d) surface and (e-g) cross-section morphologies of the samples: (a) substrate, (b, e) Sr/F-CaP-400, (c, f) Sr/F-CaP-450, (d, g) Sr/F-CaP-500

The chemical compositions of the samples are summarized in Table 2. The substrate is composed of 97.45 Mg, 2.03 Zn and 0.52 Mn (in at.%), whose chemical composition is close to the Mg-4Zn-1Mn alloy. For the MAO coatings, their chemical compositions include O, Mg, P major elements and Na, F, Ca, Zn, Ca, Sr minor elements, indicating that the Sr/F containing CaP coatings are deposited on the substrate surface.

Table 2 Chemical compositions of the samples (in at.%)

Samples	Mg	Zn	Mn	O	Sr	F	Ca	P	Na
Substrate	97.45	2.03	0.52	—	—	—	—	—	—
Sr/F-CaP-400	24.00	0.58	—	60.39	0.15	1.41	0.31	10.99	2.17
Sr/F-CaP-450	23.99	0.31	—	59.74	0.13	1.20	0.17	12.13	2.33
Sr/F-CaP-500	22.71	0.21	—	61.13	0.15	1.08	0.29	12.49	1.94

3.2 Corrosion behavior

Figure 2 demonstrates the EIS results of the samples in SBF at 37 °C. As shown in Figure 2a, the Nyquist plots of the samples consist of two parts: a capacitive reactance arc in the high-frequency region and an inductive reactance arc in the low-frequency region. Usually, a larger arc implies a higher anti-corrosion ability [29-30]. The MAO coatings exhibit larger capacitive reactance arc and inductive reactance arc than those of the substrate, suggesting that the former samples possess better corrosion resistance. The equivalent circuit for the

Nyquist plots is shown in Figure 2b and the fitting data are listed in Table 3. Here, the R_s is the solution resistance. The CPE_1 and CPE_2 represent the capacitive response of the corrosion products layer and the capacitance value at the solution/substrate interface, respectively. The R_1 and R_2 refer to the resistance of corrosion products layer (outer layer) and the charge transfer resistance (inner layer), respectively. It is noted that the samples have a higher R_2 value and a lower R_1 value, which demonstrates that the inner layer has a greater effect on the corrosion resistance than the outer layer. A similar result can also be found in the reference[31]. The R_p (R_1+R_2) can be used to evaluate the corrosion resistance of the samples, which increases in the order of substrate (511.0 Ω cm^2) $<$ Sr/F-CaP-400 (2150.1 Ω cm^2) $<$ Sr/F-CaP-500 (2887.3 Ω cm^2) ≈ Sr/F-CaP-450 (2830.3 Ω cm^2).

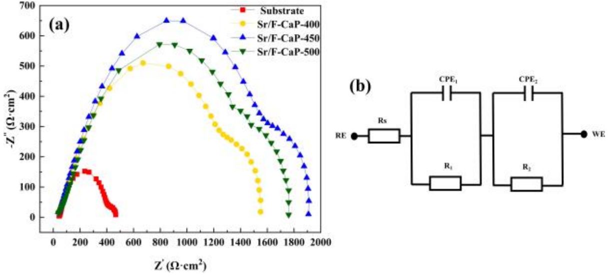

Figure 2 EIS results of the samples in SBF at 37 °C: (a) Nyquist plots, (b) equivalent circuit

Figure 3 presents the PDP curves of the samples in SBF at 37 °C. The electrochemical parameters fitted from the PDP curves are listed in Table 4. Generally, the E_{corr} represents the anti-corrosion ability of the coating and the i_{corr} indicates the corrosion rate once corrosion happens. A combination of larger E_{corr} and smaller i_{corr} usually stands for a better corrosion behavior[32]. The E_{corr} value of the substrate is about -1.570 V/SCE, while the E_{corr} value of the MAO coatings shows a slightly positive shift to -1.465 V/SCE, -1.502 V/SCE and -1.469 V/SCE for the Sr/F-CaP-400, Sr/F-CaP-400 and Sr/F-CaP-400 samples, respectively. Furthermore, the i_{corr} value increases in the order of Sr/F-CaP-450 (1.01×10^{-6} A cm^{-2}) ≈ Sr/F-CaP-400 (1.10×10^{-6} A cm^{-2}) $<$ Sr/F-CaP-500 (1.94×10^{-6} A cm^{-2}) $<<$ substrate (5.69×10^{-5} A cm^{-2}). This suggests that the MAO coatings can improve the corrosion behavior of Mg alloy to some extent. Similar results have been obtained by Shang et al [33].

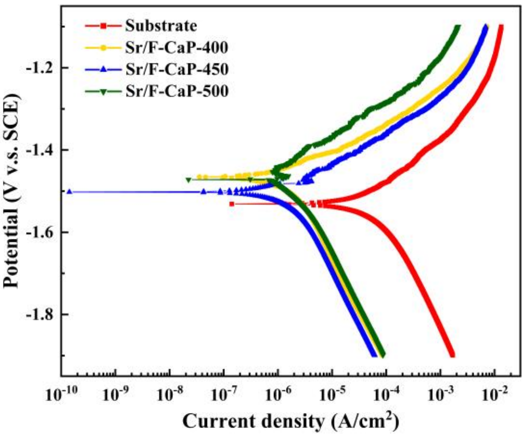

Figure 3 PDP curves of the samples in SBF at 37 °C

Table 4 Electrochemical parameters of corrosion potential (E_{corr}) and corrosion current density (i_{corr}) fitted from the PDP curves

Samples	E_{corr} (V/SCE)	i_{corr} (A cm^{-2})
Substrate	-1.570	5.69×10^{-5}
Sr/F-CaP-400	-1.465	1.10×10^{-6}
Sr/F-CaP-450	-1.502	1.01×10^{-6}
Sr/F-CaP-500	-1.469	1.94×10^{-6}

Figure 4 displays the corrosion morphologies of the samples after immersion in SBF at 37 °C for 2, 6, 14 days. After 2 days immersion, the substrate surface is obviously corroded to show lots of cracks (Figure 4a). From Figure 4b-4d, the surfaces of MAO coatings suffer varying degrees of corrosion. Comparatively, the corroded surfaces of MAO coatings remain relatively intact, which is evidenced from the compact morphology underneath the upper corrosion products layer. After 6 days immersion, the substrate surface is filled with deep corrosion cracks and variously sized corrosion fragments, which implies a corrosion tendency to the depth direction (Figure 4e). From Figure 4f-4h, the surfaces of MAO coatings exhibit a compact and uniform corrosion morphology. The corrosion cracks formed after 2 days immersion become less and smaller due to the deposition of corrosion products layer. It is noted that the surface of Sr/F-CaP-500 sample still remains some crater-like holes, suggesting that its MAO coating is not completely corroded during 6 days immersion. In addition, corrosion continues as the immersion time further increases to 14 days. The substrate surface is covered by randomly distributed

Table 3 Fitting data of the EIS results

Samples	R_s (Ω·cm^2)	CPE_1 (Ω^{-1} cm^{-2} s^{-n})	n_1	R_1 (Ω·cm^2)	CPE_2 (Ω^{-1} cm^{-2} s^{-n})	n_2	R_2 (Ω cm^2)	R_p (Ω cm^2)
Substrate	45.36	2.35×10^{-5}	0.80	122.0	7.57×10^{-4}	0.77	389	511.0
Sr/F-CaP-400	34.90	2.01×10^{-5}	0.66	521.1	9.18×10^{-5}	0.99	1629	2150.1
Sr/F-CaP-450	34.76	1.22×10^{-5}	0.68	890.3	5.63×10^{-5}	0.80	1997	2887.3
Sr/F-CaP-500	41.11	2.65×10^{-5}	0.64	887.3	5.73×10^{-5}	0.84	1943	2830.3

irregular corrosion products (Figure 4i). From Figure 4j-4l, there exist many blocky corrosion products on the corroded surfaces of MAO coatings. The blocky corrosion products tend to form a protective layer under higher voltage, which could retard further corrosion for the substrate.

Figure 5 illustrates the changes in pH value of the SBF and weight loss/weight loss rate of the samples during immersion corrosion tests. As shown in Figure 5a, the pH value of SBF increases rapidly in initial immersion period and then increases slowly in subsequent immersion period for all the four samples. The final pH value of SBF increases in the order of Sr/F-CaP-500 (7.71) ＜ Sr/F-CaP-450 (7.81) ＜ Sr/F-CaP-400 (7.87) ＜ substrate (8.12). This increase in pH value of SBF is owing to the solution alkalization. As reported in the reference [34], both corrosion of Mg ($Mg + 2H_2O = Mg(OH)_2 + H_2$) and hydration of MgO ($MgO + 2H_2O = Mg(OH)_2$) exist on the surface of Mg alloys immersed in the corrosive media of SBF. The above reactions release abundant OH^- into the solution, which leads to the increase in pH value of SBF. An obvious reduction in pH value of SBF is observed for the MAO coatings compared with the substrate sample, indicating that the corrosion rate of Mg alloy is mitigated after MAO treatment. As shown in Figure 5b, the weight loss of samples increases with increasing immersion time, suggesting that corrosion continues during the immersion duration. After 14 days immersion time, the average weight loss increases in the order of Sr/F-CaP-500 (10.06 mg/cm^2) ＜ Sr/F-CaP-450 (11.72 mg/cm^2) ≈ Sr/F-CaP-400 (12.23 mg/cm^2) ＜ substrate (17.45 mg/cm^2) and it is reduced by 57.65%, 67.16% and 70.09% in comparison with that of substrate. Moreover, the weight loss rate of samples has a descending tendency as the immersion time increases, implying that the corrosion products layer has some protective effect on the substrate. At the end of 14 days immersion time, the average weight loss rate increases in the order of Sr/F-CaP-500 (0.72 mg/cm^2/day) ＜ Sr/F-CaP-450 (0.84 mg/cm^2/day) ≈ Sr/F-CaP-400 (0.87 mg/cm^2/day) ＜ substrate (1.25 mg/cm^2/day).

Figure 6 shows the SEM-EDS analysis of the corrosion products on the surface of substrate and Sr/F-CaP-500 samples after immersion in SBF for 14 days. The Sr/F-CaP-500 sample with the lowest corrosion rate is selected to investigate the corrosion products with the substrate sample being the control. In Figure 6a, the corrosion products on the surface of substrate exhibits coarse granular shape, whose composition is composed of 49.89 O, 1.67 Na, 8.04 Mg, 15.53 P, 23.06 Ca, 0.64 Mn and 1.17 Zn (in wt.%). In Figure 6b, the corrosion products on the surface of Sr/F-CaP-500 sample exhibits tiny acicular shape, whose composition is composed of 56.99 O, 34.79 Mg, 1.41 P and 6.82 Cl (in wt.%). The existence of MAO coating alters the formation process of corrosion products layer, which results in an improved corrosion behavior to some extent.

Figure 7 shows the schematic diagrams of possible corrosion mechanisms before and after MAO treatment. From Figure 7a, the substrate with a strong chemical activity easily reacts with H_2O in SBF to form $Mg(OH)_2$ and generate H_2. The $Mg(OH)_2$ is unstable and can react with corrosive ions like Cl^- to form soluble $MgCl_2$. After corrosion, there appear various corrosion pits on the surface. From Figure 7b, the MAO coatings can protect the substrate from corrosion in the initial corrosion period. As corrosion progresses, some random corrosion pits are formed on the MAO coatings, which gives a few passages for corrosive media and induces the corrosion of substrate. Because of the bilayer structure of MAO coatings (dense inner layer and porous outer layer), there tends to deposit more uniform and compact corrosion products layer on the surface. In summary, the MAO coatings can block the corrosive media from reaching the substrate and they also have good corrosion resistance, which retards the corrosion of substrate in the initial corrosion period.

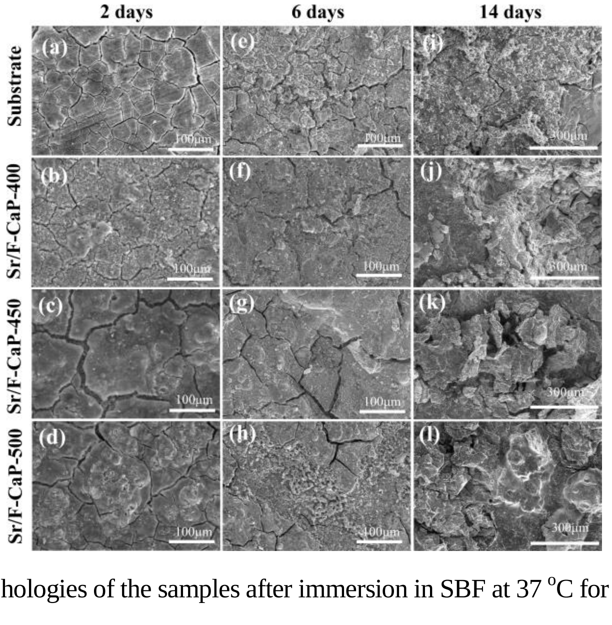

Figure 4 Corrosion morphologies of the samples after immersion in SBF at 37 °C for 2 days, 6 days and 14 days

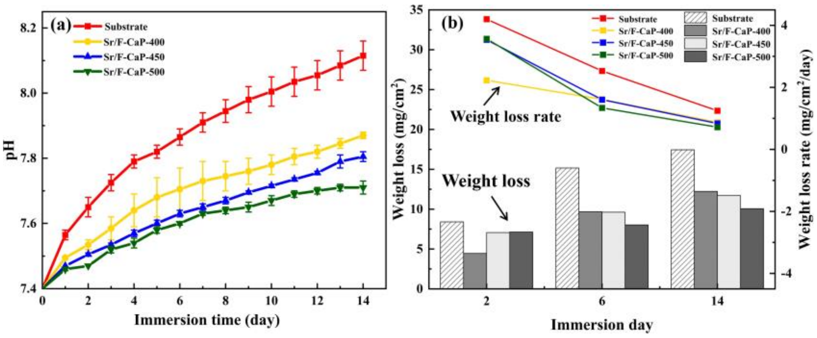

Figure 5 Changes in (a) pH value of the SBF, (b) weight loss/weight loss rate of the samples during immersion corrosion tests

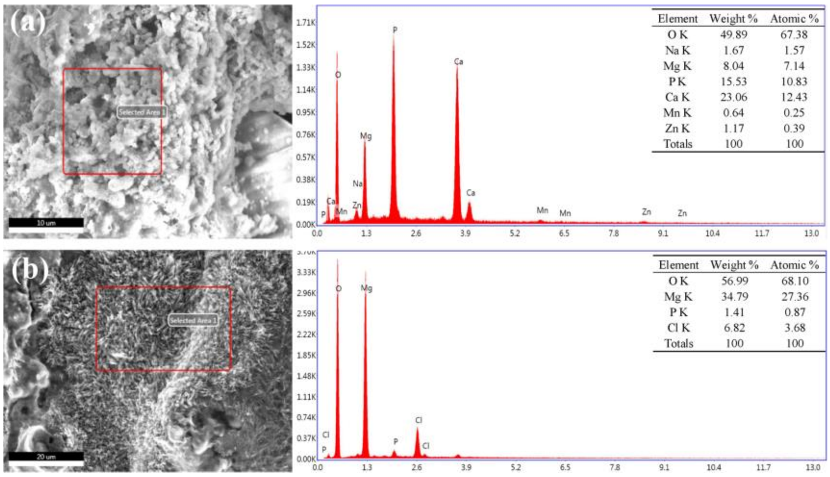

Element	Weight %	Atomic %
O K	49.89	67.38
Na K	1.67	1.57
Mg K	8.04	7.14
P K	15.53	10.83
Ca K	23.06	12.43
Mn K	0.64	0.25
Zn K	1.17	0.39
Totals	100	100

Element	Weight %	Atomic %
O K	56.99	68.10
Mg K	34.79	27.36
P K	1.41	0.87
Cl K	6.82	3.68
Totals	100	100

Figure 6 SEM-EDS analysis of the corrosion products on the surface of (a) substrate, (b) Sr/F-CaP-500 after immersion in SBF for 14 days

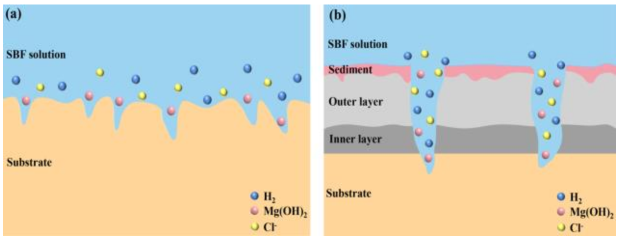

Figure 7 Schematic diagrams of possible corrosion mechanisms: (a) before and (b) after MAO treatment

It should be pointed out that there exists a certain disagreement in corrosion rate of the same sample between electrochemical corrosion result and immersion corrosion result. The best corrosion resistance is found for the Sr/F-CaP-450 sample and Sr/F-CaP-500 sample with respect to electrochemical corrosion tests and immersion corrosion tests, respectively. The reasons can be ascribed to the following two reasons: Firstly, the electrochemical corrosion tests are non-equilibrium and short-term corrosion evaluation method. Their results are mainly determined by the surface passivation that are affected by the cracks, holes, chemical compositions, etc. Secondly, the immersion corrosion tests are equilibrium and long-term corrosion evaluation method. Their results are influenced by the stability of corrosion products layer. Overall, the Sr/F-CaP MAO coatings fabricated under 450-500 V possess better corrosion resistance, which can provide the substrate a better protective effect.

4 Conclusion

The microstructure and corrosion behavior of Mg-4Zn-1Mn alloy surface modified by Sr/F-CaP MAO coatings have been studied. The main conclusions are as follows:

(1) The Sr/F-CaP MAO coatings bonded well with the Mg-4Zn-1Mn alloy. They exhibited uneven crater-like holes and tiny cracks under 400 V voltage and showed relatively homogeneous crater-like holes without cracks under 450 V and 500 V voltages. The thickness of MAO coatings increased from 7.8 μm to 11.0 μm as the voltage increased from 400 V to 500 V.

(2) The short-term corrosion behavior evaluated by electrochemical corrosion tests indicated that the MAO coatings could reduce the corrosion rate of substrate. The Sr/F-CaP-450 sample with the largest R_p value (2830.3 Ω cm^2) and smallest i_{corr} value (1.01×10^{-6} A cm^{-2}) had the lowest corrosion rate.

(3) The long-term corrosion behavior assessed by immersion corrosion tests demonstrated that the

corrosion resistance of substrate could be enhanced by the MAO coatings. The Sr/F-CaP-500 sample with the smallest weight loss (10.06 mg/cm^2) and weight loss rate (0.72 mg/cm^2/day) after 14 days immersion time exhibited the best corrosion resistance.

Author Contributions: Weirong Li: Investigation, Writing – review & editing. Yanfang Li: Investigation. Qian Li: Investigation. Xuan Xiong: Investigation. Fangfei Liu: Investigation. Ronghui Li: Investigation. Heng Li: Investigation. Dong Pang: Investigation. Jia Lu: Writing – review & editing. Xuan Zhang: Investigation, Writing – original draft.

Acknowledgements: This work did not receive any specific grant from funding agencies in the public, commercial, or not-for-profit sectors.

Declaration of Competing Interest: No potential conflicts of interest.

References

[1]Tsakiris V, Tardei C, Clicinschi F M. Biodegradable Mg alloys for orthopedic implants–A review[J]. Journal of Magnesium and Alloys, 2021, 9(6):1884-1905.

[2]Espiritu J, Meier M, Seitz J M. The current performance of biodegradable magnesium-based implants in magnetic resonance imaging: A review[J]. Bioactive Materials, 2021, 6(12):4360-4367.

[3]Song M S, Zeng R C, Ding Y F, et al.. Recent advances in biodegradation controls over Mg alloys for bone fracture management: A review[J]. Journal of materials science & technology, 2019, 35(4): 535-544.

[4]Liang J, Lei Z, Chen Y, et al.. Microstructure evolution of laser powder bed fusion ZK60 Mg alloy after different heat treatment[J]. Journal of Alloys and Compounds, 2022, 898: 163046.

[5]Ling L, Cai S, Li Q, et al.. Recent advances in hydrothermal modification of calcium phosphorus coating on magnesium alloy[J]. Journal of Magnesium and Alloys, 2022,10(1):62-80.

[6]Amukarimi S, Mozafari M. Biodegradable magnesium‐based biomaterials: An overview of challenges and opportunities[J]. MedComm, 2021,2(2):123-144.

[7]Zerankeshi M M, Alizadeh R, Gerashi E, et al.. Effects of heat treatment on the corrosion behavior and mechanical properties of biodegradable Mg alloys[J]. Journal of Magnesium and Alloys, 2022(21):78-82.

[8]Wei X, Liu P, Ma S, et al.. Improvement on corrosion resistance and biocompability of ZK60 magnesium alloy by carboxyl ion implantation[J]. Corrosion Science, 2020(173):108729.

[9]Yiu P, You J D, Wang S T, et al.. Tunable hydrophilicity in a surface nano-textured stainless steel thin film deposited by DC magnetron sputtering[J]. Applied Surface Science, 2021(555):149705.

[10]Jothi V, Adesina A Y, Kumar A M, et al.. Enhancing the biodegradability and surface protective performance of AZ31 Mg alloy using polypyrrole/gelatin composite coatings with anodized Mg surface[J]. Surface and Coatings Technology, 2020(381):125139.

[11]Rahman M, Li Y, Wen C. HA coating on Mg alloys for biomedical applications: A review[J]. Journal of Magnesium and Alloys, 2020,8(3):929-943.

[12]Li W, Su Y, Ma L, et al.. Sol-gel coating loaded with inhibitor on ZE21B Mg alloy for improving corrosion resistance and endothelialization aiming at potential cardiovascular application[J]. Colloids and Surfaces B: Biointerfaces, 2021(207): 111993.

[13]Wang T, Xu Y, Zhang Q, et al.. Enhancing the antibacterial properties of magnesium alloys with copper-doped anhydrous calcium phosphate nanoparticles embedded into the polycaprolactone coating for medical implants[J]. ACS Applied Nano Materials, 2022,5(12):18965-18976.

[14]Zhang K, Yu S. Preparation of wear and corrosion resistant micro-arc oxidation coating on 7N01 aluminum alloy[J]. Surface and Coatings Technology, 2020(388): 125453.

[15] Sankara Narayanan T S N , Il Song Park, Min Ho Lee. Strategies to improve the corrosion resistance of microarc oxidation (MAO) coated magnesium alloys for degradable implants: Prospects and challenges[J]. Progress in Materials Science, 2014, 60: 1.

[16]Xi K, Wu H, Zhou C, et al.. Improved corrosion and wear resistance of micro-arc oxidation coatings on the 2024 aluminum alloy by incorporation of quasi-two-dimensional sericite microplates[J]. Applied Surface Science, 2022(585):152693.

[17]Lin Z, Wang T, Yu X, et al.. Functionalization treatment of micro-arc oxidation coatings on magnesium alloys: A review[J]. Journal of Alloys and Compounds, 2021(879):160453.

[18]He R Y, Wang B Y, Xiang J H, et al.. Effect of copper additive on microstructure and anti-corrosion performance of black MAO films grown on AZ91 alloy and coloration mechanism[J]. Journal of Alloys and Compounds, 2021(889):161501.

[19]Ly X N, Yang S. Influence of current mode on microstructure and corrosion behavior of micro-arc oxidation (MAO) biodegradable Mg-Zn-Ca alloy in Hank's solution[J]. Surface and Coatings Technology, 2019(358):331-339.

[20]Lin Xiao, Tan Lili, Zhang Qiang, et al.. The in vitro degradation process and biocompatibility of a ZK60 magnesium alloy with a forsterite-containing micro-arc oxidation coating[J]. Acta Biomaterialia, 2019,9(10):8631–8642.

[21]Zhu H, Li X, Guan X, et al.. Effect of molybdate conversion coating of magnesium alloy reinforced by micro-arc oxidation[J]. Metals and Materials International, 2021(27):3975-3982.

[22]Chaharmahali R, Fattah-alhosseini A, Babaei K. Surface characterization and corrosion behavior of calcium phosphate (Ca-P) base composite layer on Mg and its alloys using plasma electrolytic oxidation (PEO): A review[J]. Journal of Magnesium and Alloys, 2021,9(1):21-40.

[23]Liu P, Wang J M, Yu X T, et al.. Corrosion resistance of bioinspired DNA-induced Ca–P coating on biodegradable magnesium alloy[J]. Journal of Magnesium and Alloys,

2019, 7(1): 144-154.

[24]Zhang Z Y, Huang T Y, Zhai D J, et al.. Study on strontium doped bioactive coatings on titanium alloys surfaces by micro-arc oxidation[J]. Surface and Coatings Technology, 2022(451):129045.

[25]Yu W, Sun R, Guo Z, et al.. Novel fluoridated hydroxyapatite/MAO composite coating on AZ31B magnesium alloy for biomedical application[J]. Applied Surface Science, 2019(464):708-715.

[26]Zheng Y, Zang L, Bi Y, et al.. Corrosion behavior of Fe/Zr composite coating on ZK60 Mg alloy by ion implantation and deposition[J]. Coatings, 2018,8(8):261.

[27]Küçükosman R, Şüküroğlu E E, Totik Y, et al.. Investigation of wear behavior of graphite additive composite coatings deposited by micro arc oxidation-hydrothermal treatment on AZ91 Mg alloy[J]. Surfaces and Interfaces, 2021(22): 100894.

[28]Yao J, Wang Y, Wu G, et al.. Growth characteristics and properties of micro-arc oxidation coating on SLM-produced TC4 alloy for biomedical applications[J]. Applied Surface Science, 2019(479):727-737.

[29]Jiang S, Zhang Z, Wang D, et al.. ZIF-8-based micro-arc oxidation composite coatings enhanced the corrosion resistance and superhydrophobicity of a Mg alloy[J]. Journal of Magnesium and Alloys, 2021(233):480-485.

[30]Xue K, Liang L X, Cheng S C, et al.. Corrosion resistance, antibacterial activity and drug release of ciprofloxacin-loaded micro-arc oxidation/silane coating on magnesium alloy AZ31[J]. Progress in Organic Coatings, 2021(158):106357.

[31]Kaseem M, Hussain T, Rehman Z U, et al.. Stabilization of AZ31 Mg alloy in sea water via dual incorporation of MgO and WO3 during micro-arc oxidation[J]. Journal of Alloys and Compounds, 2021(853):157036.

[32]H Wu Z, Shi X Zhang, A M Qasim, et al.. Achieving an acid resistant surface on magnesium alloy via bio-inspired design[J]. Applied Surface Science, 2019 (4789):150-161.

[33]Shang W, Wu F, Jiang S, et al.. Effect of hydrophobicity on the corrosion resistance of microarc oxidation/self-assembly/nickel composite coatings on magnesium alloys[J]. Journal of Molecular Liquids, 2021(330):115606.

[34]Xu W, Liu Z, Li B, et al.. Effects of magnetic field force in preparation of plasma electrolytic oxidation coatings: A novel method to improve the corrosion resistance of magnesium[J]. Journal of Alloys and Compounds, 2022(906):162642.

Viser Technology Pte. Ltd.
Research and Application of Materials Science
DOI: 10.33142/rams.v5i2.12705

Research Article Open Access

The Influence of Dry or Wet Activating Process to the Electrochemical Features of Biowaste Carbon

Zhonghe SONG[1], Yanmei ZHAO[2], Shangwen MA[3], Tiezhen REN [1, 3*]

1. School of Chemical Engineering, Xinjiang University, Urumqi, Xinjiang, 830046,China
2. School of Chemical Engineering, Hebei University of Technology, Tianjin, 300130, China
3. Bayingol Vocational and Technical School, Korla, Xinjiang, 841000, China

[*]***Corresponding Author:*** *Tiezhen REN, E-mail: rtz@xju.edu.cn*

Abstract

The utilization of biowaste to the activated carbon (AC) as electrode material is conducive to alleviating the energy crisis and promoting the high value-added. The popular KOH activation has been applied for years, but rare report clarified the difference of dry and wet activation, with which the batch producing technique could be different. Here nitrogen doped hierarchical AC was derived from wood chip by a wet or dry KOH activation. The surface area, framework structure and surface feature were characterized to reveal the effect of wet and dry activation. 1.44 at% of nitrogen doped AC was made by dry KOH activation, which was higher than the AC derived from wet KOH activation with 1.36 at% of nitrogen. Their electrochemical properties were investigated in 6 mol L^{-1} of KOH, the capacitance of wAC was 401 F g^{-1} at 0.5 A g^{-1}, but dAC possessed a capacitance of 215 F g^{-1}. These indicated that AC obtained by using wet KOH activation displayed a potential application in energy field.

Keywords: *Activated carbon; KOH activation process; supercapacitor*

1 Introduction

Biowaste-derived activated carbon (AC) has been widely used in adsorbents[1,2], electrocatalysts[3,4] and other fields with possessed features, such as high specific surface area, flexible pore size distribution and adjustable surface features with heteroatoms[5]. Specially, their functional groups and morphological characteristics are closely related to the electrochemical performance by enhancing the diffusion of electrolyte ions [6]. As a double-layer capacitance, the cycle life of AC electrode is often higher than the metal oxides, which was ascribed to the pseudocapacitor [7]. It is confirmed that the micropores determine the space for charge storage and the reasonable pore structures decide the kinetics of current charging and discharging [8]. While, to meet the demand for industrial mass production the technology challenges the activation process of KOH.

Some reports adopted dry-mixing or wet-mixing KOH activation to obtain the AC [9-10]. Under the premise of ensuring catalysts active, a higher requirement is putting forward to reducing the amount of KOH. By 9 mass ratio of wet KOH activation, AC derived from willow wood displayed a surface area of 2800 m^2 g^{-1} and a capacitance of 394 F g^{-1} at 1 A g^{-1}[9]. The Celery-derived AC with polyaniline as a nitrogen source was prepared by four-times of KOH solution[11], which capacitance could reach to 402 F g^{-1} in H_2SO_4 (1 mol L^{-1}) at 1 A g^{-1}. However, the differences of microporous structure and functional group contents in carbon might affect the electrochemical feature and the biomass sources are unique with a specific activation process for their own [12]. It is still in question for limiting the consumption of KOH and finding a matched activation technique.

Here, KOH activation by dry or wet mixing have been chosen to construct nitrogen doped AC from wood chip. The physical feature was characterized and the pore structure was discussed to illustrate the effect of activation process. The related capacitance was evaluated with cyclic voltammetry (CV) test and charging-discharging performance in a two-electrode system. The results could highlight the activating technique for batch production of AC in the future.

2 Experimental Details

All the chemicals purchased from Sigma Aldrich Co.

Received on October 6, 2023; Accepted on November 14, 2023

Ltd was directly used without any pretreatment. Wood chip was collected from Korla, Xinjiang and cleaned with water to remove the surface dust.

2.1 Preparation process

First, 5 g of wood chip was carbonized in nitrogen flow (60 mL min^{-1}) in a tube furnace at 500 ℃ for 2 h, for which 10 ℃ min^{-1} of rate was kept from room temperature to final. Then the collected sample was mixed with two mass ratios of KOH. For wet KOH activation, 20 ml of distilled water was added and stirred overnight for 12 h, following the activation was set at 800 ℃ for 2 h with same setting program. For dry KOH activation, the KOH is fully grinded with the carbonized AC for half an hour. After activation, all the samples were neutralized with 1 mol L^{-1} of HCl and distilled water. Finally, drying them in the oven at 80 ℃ and the collected sample was named wAC and dAC, respectively.

2.2 Characterizations

To understand the porous feature of the sample, nitrogen adsorption-desorption isotherms analyzer (Quantachrome Autosorb-1 MP) were taken at liquid-N_2 temperature (-196 ℃). The surface area was calculated by Brunauer-Emmett-Teller (BET) method and pore size distribution was deduced by Non-Local Density Functional Theory (NLDFT) [13]. The morphology of the samples was observed from scanning electron microscope (SEM, JSM-6490LV); Transmission electron microscope (TEM, JEM 1010) was used to record the microstructure. Raman scattering spectra were recorded by Renishaw InVia with 532 nm excitation light source. To reveal the detail surface structure, the X-ray photoelectron spectroscopy (XPS, Thermo ESCALAB 250) was taken with irradiation source monochromatic Al Kα radiation (150 W, 15 kV, and 1486.6 eV) in an evacuated chamber ($5.2*10^{-9}$ mbar). High resolution spectra were performed to explore the local environment of each element at a fixed angle of 90 °. C1s (284.6 eV) was used to calibrate the energy scale.

2.3 Electrochemical tests

Nickel foam was selected as working electrode collector with 1cm^2 active area. Ethanol was used as the dispersible solvent. 10 mg of sample was first mixed with acetylene black and polytetrafluoroethylene (60 wt%), by keeping a mass ratio of 75:25:5. Then the mixture was pressed under 20 MPa for 20 s to form the electrode. Before test, the work electrode was fully infiltrated in KOH electrolyte (6 mol L^{-1}) for 10 h. The galvanostatic discharge-charge cycling tests were measured on LAND testing system.

Cyclic voltammetry (CV, -1 to 0 V) and electrochemical impedance spectroscopy (EIS, 10 mHz to 100 kHz) were tested by an electrochemical workstation (IM6&ZENNIUM). Three electrode system was designed with a reference electrode Hg/HgO and the counter electrode was a platinum electrode in KOH electrolyte (6 mol L^{-1}). EIS was recorded at open circuit voltage under disturbance voltage of 5 mV.

The specific capacitance of the two-electrode system was obtained with the equation (1). The energy density (*E*) and power density (*P*) were derived from the equation (2) and (3).

Equation:

$$\boldsymbol{C = \frac{2I\Delta t}{m\Delta V}} \tag{1}$$

$$\boldsymbol{E = \frac{1}{2*3.6} C\Delta V^2} \tag{2}$$

$$\boldsymbol{P = \frac{3600E}{\Delta t}} \tag{3}$$

Where *C* (F g^{-1}) relates to the specific capacitance, *I* (A) is the electric current, Δt (s) is the discharge time, *m* (g) is the mass of active carbon, ΔV (V) is potential difference, *E* (Wh kg^{-1} is energy density, *P* (W kg^{-1}) is power density.

3 Results and Discussions

N_2 adsorption-desorption isotherm was shown in Figure 1a. The calculated S_{BET} of wAC is 1793 m^2 g^{-1} with the total volume (V_{total}) of 1.045 cm^3 g^{-1}. While, S_{BET} of dAC is 1429 m^2 g^{-1} with the V_{total} of 0.703 cm^3 g^{-1}. According to the NLDFT method[13], the pore size distribution of wAC mainly locates at around 0.59 and 1.67 nm. For dAC, the pore size is around 0.59 nm and 1.48 nm, as represented in Figure 1b. The results indicate that wet KOH activation could be helpful to obtain the carbon with a higher SSA and larger pore volume than dry KOH activation. We believe that, due to the KOH solution is fully impregnated into the pores of the carbonized material, wAC with a richer microporous structure. Raman spectra revealed the structure of AC with the ratio of G band (1600 cm^{-1} fitting to graphite structure, sp^2) and D band (1350 cm^{-1} fitting to amorphous structure, sp^3)[14]. As represented in Figure 1c, more defects exist in wAC corresponding to the I_D/I_G values of 1.07 (dAC with 1.05), which confirm that the wet KOH causes more amorphous carbon structure than that through dry activation. The pores in carbon framework could be immersed thoroughly with KOH solution. The SEM images of dAC displayed an irregular structure like megalithic array (Figure 1d). But wAC showed a cauliflower-like morphology (Figure 1e), suggesting that the activation in solution is vigorous comparing to grinding way. TEM images display the irregular micropores as shown in Figure 1f and 1g. The related inset images clearly show that the abundant pore structure in wAC.

The function groups of the samples were

investigated by XPS (Figure 2a). The elements of C1s, N1s and O1s existed in wAC and dAC. There are more C1s (89.49 at%) contained in dAC, which is slightly higher than wAC (88.79 at%). dAC has 9.06 at% O1s less than wAC (9.85 at%). High content of nitrogen is formed during dry KOH activation (1.44 at%), comparing to wAC (1.35 at%). The C 1s spectra of the samples at around 284.6, 285.5, 286.8 and 289.1 eV are assigned into four bonding configurations, C=C, C-O/C-N, C=O/C=N and O-C=O, as represented in Figure 2b. The O1s core energy level spectra is at around 531.5, 532.5, 533.7, and 534.7 eV, fitting to the group of O=C, O-C, O-N, and water or chemisorbed O_2/CO_2 [15] in Figure 2c.

N1s spectra in Figure 2d, is at around 398.8, 399.8, 401.6 and 403.1 eV, which represent four groups of pyridine-N, pyrrole-N, graphitic-N and pyridine N^+-O^-. The wet activation process may introduce more pyrrolic-N (0.65 at%). While dry activation represents more pyridine-N (0.69 at%) and no pyridine N^+-O^- groups. This suggests that the activation process not only affect the surface feature and porous structure, the nitrogen species might be tuned during the activation. Since the alkali solution is more thoroughly interacted with carbon atoms and more functional groups could be formed, the design on heteroatoms type might be successful. All peaks information had been summarized in Table1.

The elecochemical nature of dAC and cAC was discussed through the CV curves. The large square area is obvious for wAC, indicating that rich micropores in wAC contribute to a good performance in electric double layer capacitance (Figure 3a, 3b).

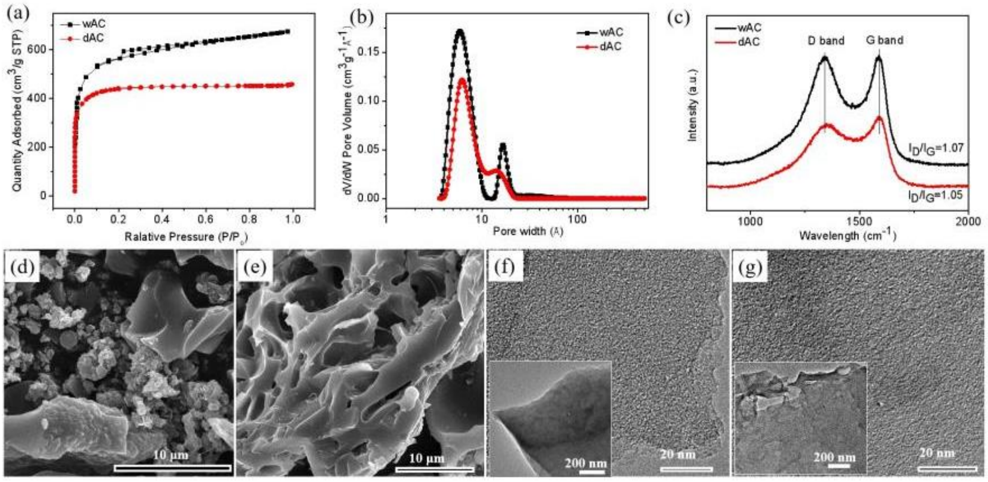

Figure 1 N_2 adsorption-desorption isotherms (a) and pore size distribution (b), Raman spectra (c), SEM images (d) and (e), TEM images (f) and (g) of dAC and wAC

Table 1 The summary of quantitative elements and the fitting peak information of the wAC and dAC by XPS

Bond assignment	Binding energy (eV)	wAC (at.%)	dAC (at.%)
C1s		88.79	89.49
C=C sp^2	284.6	57.12	58.18
C-O (phenolic, alcoholic, ether), C–N (carbon–nitrogen structures)	285.5	8.39	8.10
O-C=O (carboxyl or ester)	286.8	10.09	9.36
π→π*, π-electrons in aromatic rings	289.1	13.19	13.85
O 1s		9.85	9.06
O=C (in carboxyl/carbonyl)	531.5	4.05	3.92
O-C (in phenol/epoxy)	532.5	3.14	2.55
N-O	533.7	1.83	1.60
Water or chemisorbed O_2, CO_2	534.7	0.83	0.99
N 1s		1.36	1.44
pyridine-N	398.8	0.30	0.69
pyrrole-N	399.8	0.65	0.48
graphitic-N	401.6	0.27	0.27
pyridine N^+-O^-	403.1	0.14	---

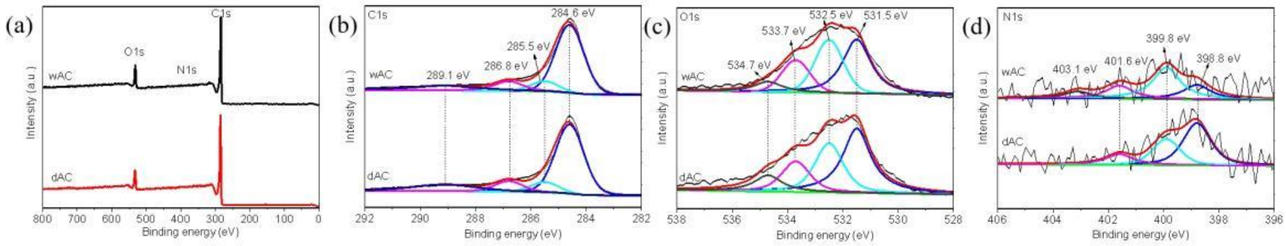

Figure 2 The XPS survey spectra (a) and high-resolution core energy level spectra of C1 (b), O1s (c), and N1s (d) of dAC and wAC

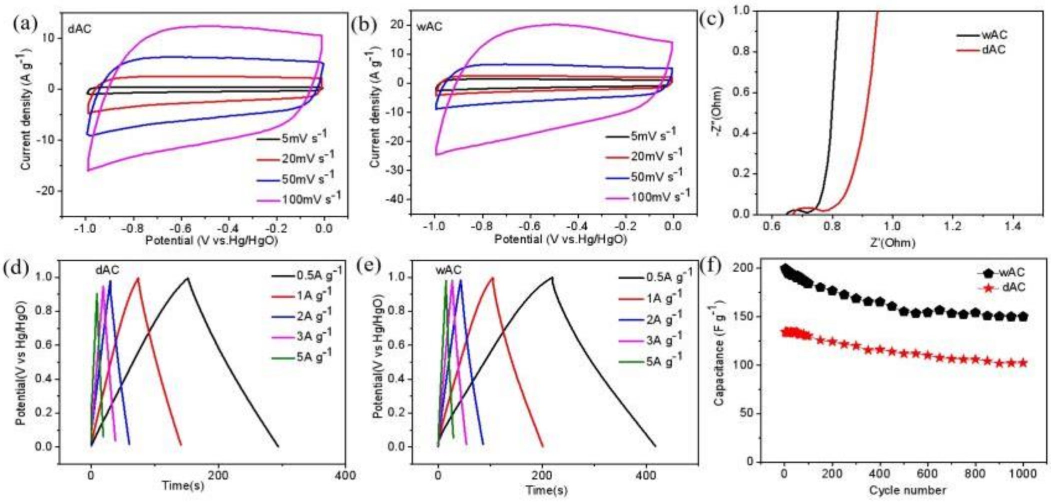

Figure 3 Cyclic voltammetry (CV) curves of dAC (a) and wAC (b), the Nyquist plots in a three-electrode system of dAC and wAC (c), the GCD curves of dAC (d) and wAC (e) in a two-electrode cell, the cycle life test at1A g^{-1} of dAC and wAC (f)

The EIS was recorded at the open circuit voltage in Nyquist plot (Figure 3c). The curves of the samples display a semi-arc and a straight line, which might be ascribed to the dynamic processes of charge transfer and mass transfer[16]. The wAC possesses a small semicircle diameter than dAC, indicating a low electrical resistance and good electrical conductivity. This must be contributed by microporous structure and nitrogen doped. Then the two-electrode system of the GCD tests were recorded in 6 mol L^{-1} of KOH. the curves in Figure 3d and 3e keep the typical triangular shape at different current density. It is obvious that the wAC shows a long charging-discharging time. The calculated capacitance of wAC and dAC from equation (1) is 200 and 134 F g^{-1} at 1 A g^{-1}. The capacitance of the samples is comparable with some literatures [17-21], which are summarized in Table 2. We may see that bio-precursors possess different surface area and capacitance even with same activating dosage. Thus, preparing AC with electrochemical feature needs to load a specific procedure for their own.

The related energy density and power density were obtained from equation (2) and (3). The wAC has a high energy density of 55 Wh kg^{-1} and power density of 1980 W kg^{-1}. This result is better than mesopores AC with Black locust seed dregs as the carbon source, its energy density is 26.2 Wh kg^{-1} and power density is 790 W kg^{-1}[22]. Cyclic stability was measured by GCD at 1 A g^{-1}. From Figure 3f, wAC electrode has the capacitance retention 75.5% after 1000 cycles GCD test, and the nearly capacitance retention 76.1% in dAC. Obviously, dry mixing is inadequate in contacting the inner surface of carbon [23]. The wet mixing activation consumes an immersion residence time, that may guarantee the carbon precursor sufficiently absorb KOH to create a functional carbon material.

Table 2 Summary of capacitance performances of carbon materials reported in various literature studies in 6 mol L^{-1} of KOH at three electrode system

Materials	KOH ratio*	Activating method	S_{BET} (m^2 g^{-1})	C (F g^{-1}) #	Refs.
Soy root	4	wet	2690	328	[17]
Natural casings	4	wet	2512	290	[18]
White sugar	3	wet	713	242	[19]
pectin	2	wet	2928	338	[20]
Tea leaves	2	dry	912	167	[21]
Wood chips	2	dry	1429	191	This work
	2	wet	1793	289	

The capacitance was recorded at 1A g^{-1}.

4 Conclusion

In this paper, nitrogen-doped AC was obtained from wood chips by wet and dry activation processes with KOH. A low surface area could be obtained during dry activation with 1429 m^2 g^{-1}, but with high content of nitrogen (1.44 at%). On the contrary, wAC possessed a surface area of 1793 m^2 g^{-1} and the nitrogen retention is1.36 at%. For nitrogen species, pyridine-N in dAC is 0.69 at%, higher than that of wAC (0.3 at%). While, pyrrole-N in dAC is 0.48 at%, lower than that of wAC (0.65 at%). As a consequence, 200 F g^{-1} could be reached for wAC, which is higher than dAC (134 F g^{-1}). Meanwhile, wAC has an energy density of 26.6 Wh kg^{-1} at a power density of 484 W kg^{-1}, which is higher than commercial activated carbon. The wet activation promotes large surface area and rich micropores. Although more nitrogen element may loss during the activation process, more oxygen-containing groups are embedded in carbon framework, which may provide predictable benefits for designing the expected carbon framework. We confirm that the wet activation method has obvious advantages over the dry activation method as an efficient bulk processing technique.

Acknowledgement: This work was supported by the Natural Science Foundation of Xinjiang Uygur Autonomous Region (2021D01A03), Project of Tian chi talent leader in Xinjiang Uygur Autonomous Region (2022).

References

[1]Lan Luo. Construction of ultra-microporous activated carbons derived from waste distiller's grains for efficient CO2 adsorption[J]. SEP PURIF TECHNOL, 2022(302):122134.

[2]Chian Ying Teo. Carbon-Based Materials as Effective Adsorbents for the Removal of Pharmaceutical Compounds from Aqueous Solution[J]. Adsorp Sci Technol, 2022(400):3079663.

[3]Xueping Sun. Novel transition-metal phosphides@N, P-codoped carbon electrocatalysts synthesized via a universal strategy for overall water splitting[J]. J. Alloys Compd, 2023(932):167253.

[4]Sanket D, Bhoyate,. Science and engineering for non-noble-metal-based electrocatalysts to boost their ORR performance: A critical review[J]. Coordin Chem Rev, 2023(474):214854.

[5]Yiliang Wang. Biomass-Derived Carbon Materials: Controllable Preparation and Versatile Applications[J]. SMALL, 2021(17): 2008079.

[6]Jiangqi Zhou. Biomass-Derived Carbon Materials for High-Performance Supercapacitors: Current Status and Perspective[J]. Electrochem. Energ Rev, 2021(4):219–248.

[7]Chunyu Zhang. Selective H2O2 Electrosynthesis over Defective Carbon from Electrochemical Etching of Molybdenum Carbide[J]. ACS Appl Mater Interfaces, 2023(15):838–847.

[8]Yunxian Zhang. Regulable pyrrolic-N-doped carbon materials as an efficient electrocatalyst for selective O2 reduction to H2O2[J]. New J Chem, 2022(46):14510-14516.

[9]Zhanyong Li. Preparation of activated carbons from poplar wood by chemical activation with KOH[J]. J Porous Mater, 2017(24):193–202.

[10]Jingjiang Liu. Promising nitrogen-rich porous carbons derived from one-step calcium chloride activation of biomass-based waste for high performance supercapacitors[J]. ACS Sustain. Chem. Eng, 2026(4):177-187.

[11]Wei Du. Nitrogen-doped hierarchical porous carbon using biomass-derived activated carbon/carbonized polyaniline composites for supercapacitor electrodes[J]. Journal of Electroanalytical Chemistry, 2018(827):213-220.

[12]Yan Zhang. Insights into the KOH activation parameters in the preparation of corncob-based microporous carbon for high-performance supercapacitors[J]. Diam Relat Mater, 2022(129):109331.

[13]John Landers. Density functional theory methods for characterization of porous materials[J]. Colloid Surface A, 2013(437):3-32.

[14]Xuelin Zhang. Heteroatom-doped porous carbons derived from moxa floss of different storage years for supercapacitors[J]. RSC Advances, 2018(8):16433-16443.

[15]hanshan Xu. Nitrogen-containing activated carbon of improved electrochemical performance derived from cotton stalks using indirect chemical activation[J]. Colloid Interface Sci, 2019(540): 285-294.

[16]Bin Wang. A simple and universal method for preparing N, S co-doped biomass derived carbon with superior performance in supercapacitors[J]. Electrochimica Acta, 2019(309):34-43.

[17]Nannan Guo. Interconnected and hierarchical porous carbon derived from soybean root for ultrahigh rate supercapacitors[J]. J Alloy Compd, 2020(834):155115.

[18]Zongying Xu. N-enriched multilayered porous carbon derived from natural casings for high-performance supercapacitors[J]. Applied Surface Science, 2018(444): 661-671.

[19]Kabir.O. Oyedotun. Examination of high porosity activated carbon obtained from dehydration of white sugar for electrochemical capacitor applications[J]. ACS Sustainable Chemistry & Engineering, 2019(7):537–546.

[20]Yuhao Zhou. In-situ template cooperated with urea to construct pectin-derived hierarchical porous carbon with optimized pore structure for supercapacitor[J]. Electrochim. Acta, 2020(355):13681.

[21] Xinyu Song. Tea waste derived microporous active carbon with enhanced double-layer supercapacitor behaviors[J]. Applied Surface Science, 2019(487):189-197.

[22]Lijie Hou. Hierarchically porous and heteroatom self-doped graphitic biomass carbon for supercapacitors[J]. Colloid Surface A, 2019(540):88-96.

[23]Pengfei Zhang. Ultrahigh surface area carbon from carbonated beverages: combining self-templating process and in situ activation[J]. Carbon, 2015(93):39-47.

Viser Technology Pte. Ltd.
Research and Application of Materials Science
DOI: 10.33142/rams.v5i2.12706

Research Article **Open Access**

Study on Gas Explosion Characteristics in Urban Utility Tunnels

Hongfu MI*, Haoliang ZHANG*, Kaixuan LIAO, Nan LUO, Huiqian LIAO

Chongqing University of Science and Technology, Chongqing, 401331, China

****Corresponding Author:*** *Hongfu MI, Haoliang ZHANG, E-mail: mimihh5@163.com, 703034980@qq.com*

Abstract

In order to study the effects of three factors, namely, premixed gas concentration, number of pressure relief ports and number of obstacles, on the overpressure characteristics of gas explosion and flame structure of gas chambers in utility tunnels, in this paper, a small and narrow experimental platform for gas explosion was constructed to study the evolution mechanism and law of the kinetic characteristics and flame behavior of gas explosion in utility tunnels, with a view to revealing the special influencing mechanism of the overpressure characteristics and flame behavior of gas explosion in utility tunnels. The results show that in the methane concentration of 9.5% when the explosion overpressure reaches its peak, and at the same time by the utility tunnel long and narrow restricted space, the explosion generated by the precursor shock wave along with the flame compression wave were superimposed on both ends of the pipeline back and forth for many times so that the overpressure waveforms are cyclic oscillatory trend, increasing the explosion hazards; compared with the closed conditions, the relief port on the overpressure characteristics of the significant impact of the maximum decrease of 57.7%, when the frequency of overpressure oscillation is reduced, the gas explosion generated by the overpressure damage is reduced; the presence of obstacles significantly affects the flow field, accelerates the flame propagation and leads to greater overpressure peaks and overpressure oscillations. The conclusions of the study can provide a basis for the safety of natural gas in utility tunnels.

Keywords: *Utility tunnels, gas explosions, explosion overpressure, overpressure oscillations, flame development*

1 Introduction

With the advancement of urban modernization, underground utility tunnels have become an important way to solve the problem of arranging various pipeline facilities [1], and gas pipelines are allowed to be included in the utility tunnel and independently into compartments [2-5]. However, in recent years, a number of gas leakage and explosion accidents in Shandong Huangdao, Kaohsiung, Taiwan, Songyuan, Jilin and other places have caused major casualties and property losses, which has sounded the alarm for the safe operation of gas compartments in utility tunnels. Therefore, how to reduce the occurrence of gas explosion accidents in utility tunnels, control the threat of gas explosion that exists at any time, and reduce the casualties and property losses that it may be caused has become one of the major topics that we urgently need to study.

Some scholars conducted experimental research on the characteristics of gas explosions and related issues in confined spaces. Wang Dongwu and Du Chunzhi [6] studied the explosion process and propagation characteristics of gas-air mixtures with different masses or concentrations. They analyzed that the peak value of the maximum explosion pressure during gas explosion is larger. Moreover, with the increase of gas volume, the position of the maximum peak pressure closer to the ignition source, and the absolute value of flame propagation speed increases significantly. Wang Quan et al. [7] studied the flame propagation characteristics of premixed methane and air gases in acrylic glass pipelines. They found that the pressure signal at the measuring point after ignition and the light signal jumped synchronously, but there was a peak pressure after the peak light moment, and the pressure duration was longer. Zheng Xingzhong et al. [8] investigated the influence of methane concentration and ignition energy on flame propagation through explosion experiments. The results showed that when the methane concentration was 10%, the explosion energy, flame propagation time, and destructive effects were the greatest. When the ignition energy was not less than 1 J, the flame length increased steadily; otherwise, the flame length would rapidly rise.

Received on October 21, 2023; Accepted on December 3, 2023

And other scholars also investigated the flame and pressure propagation characteristics during natural gas pipeline explosions [9-11].

Meanwhile, some scholars conducted experimental and simulation studies on actual engineering of utility tunnels, exploring the effects of external factors such as relief vents and obstacles on gas explosions within the tunnels. G.Tomlin [12] conducted 38 explosion experiments with a gas concentration of 9.5% to study the influence of different venting areas on the degree of container explosion damage. It was found that too small venting areas or excessively large venting valve thresholds would exacerbate the explosive damage effects. Moen [13] and Barry [14] et al. utilized a computer model combining the discrete vortex method with flame interface algorithm to study the acceleration of premixed flames propagating through stagnant obstacles in planar channels. The research findings revealed that obstacles caused a sudden contraction of airflow, resulting in initial acceleration of the flame. Combustion generated airflow forming turbulent recirculation zones downstream of the obstacles, where the flame interacted with turbulent vortices, increasing the combustion rate. Consequently, the velocity field within the channel intensified, further accelerating the flame. Jiang Jiahong [15] conducted numerical simulations of gas chamber explosions in utility tunnels using FLUENT. The results indicated that the length of accumulated premixed gas in the sealed utility tunnels had the most significant influence on the explosion intensity, while the impact of the tunnel cross-sectional shape was negligible. The size of openings in partially open utility tunnels would affect the overpressure intensity within the tunnels, with the venting effect strengthening as the opening size increased. Xu et al.[16] utilized FLACS to investigate four different designs of venting layouts while simultaneously conducting gas dispersion and explosion simulations. The research findings indicated that under the action of venting, the size of the leaked gas cloud primarily depended on the distance from the leakage point to the vent. Properly setting up venting layouts could significantly reduce the maximum explosion overpressure from 2.23 bar to 1.97 bar. Wang et al. [17] developed a numerical model for gas explosions in large tunnels. Their study revealed that gas explosions in utility tunnels could be divided into three stages based on pressure and flame development: the combustion-induced rise stage, the oscillation rise stage, and the oscillation fall stage. Furthermore, setting up side ventilation ports near the end of the tunnels could reduce peak pressure by 42%～78% and oscillation peak by 35%～87%. In summary, researchers both domestically and internationally focused their studies on the characteristics of gas explosions within confined spaces. However, unlike typical confined spaces, utility tunnels due to their elongated structure, are highly susceptible to transitioning from deflagration to detonation in the event of a gas explosion [18]. However, researchers have primarily utilized numerical simulation methods for studying the combustion and explosion characteristics of utility tunnels, lacking consideration for factors such as the complex layout of auxiliary facilities and dynamic ventilation conditions within the tunnels. Moreover, there is insufficient experimental data available. Therefore, to support accident consequence assessment and the formulation of safety protection strategies in the event of explosions in utility tunnels, there is an urgent need to conduct gas explosion experimental research that conforms to real tunnel scenarios. This will provide essential data with high confidence levels required for validating numerical computational models, thereby offering crucial insights for disaster prevention and mitigation designs in urban utility tunnels.

This study aimed to address the characteristics of gas explosions in utility tunnels. By referencing national standards and literature, key influencing factors of gas explosion characteristics in utility tunnels were identified. Subsequently, a small-scale, elongated, confined space explosion experimental platform was constructed to analyze the behavior of explosion flames and changes in overpressure characteristics under the influence of these key factors. The objective was to reveal the evolutionary patterns and mechanisms of gas explosion flame characteristics within elongated underground spaces systematically. Ultimately, this research seeks to enhance the theoretical understanding of gas explosions in elongated confined spaces and provide technical support for the safety management of gas explosion accidents in urban utility tunnels.

2 Explosion Experimental Platform

2.1 Experimental system

Due to the complexity of factors affecting methane-air explosions in elongated confined spaces, and the coupled effects among various parameters, the explosion development process is inherently complex. Describing the explosion characteristic parameters within elongated spaces is therefore challenging [19]. Therefore, this paper relied on the Oil and Gas Fire and Explosion Dynamics Laboratory, considering the spatial elongation and complex internal structure of the gas chamber in utility tunnels, constructed a small-scale elongated pipeline gas explosion experimental platform, as shown in Figure 1.

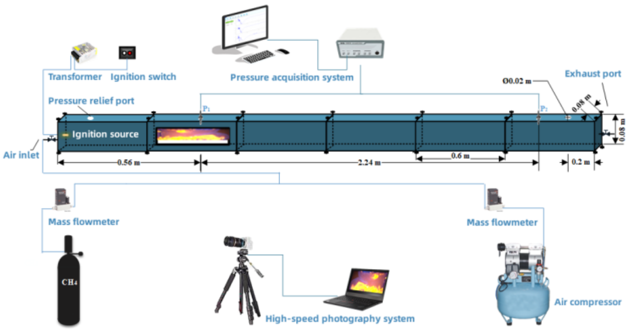

Figure 1 Schematic Diagram of the Experimental Setup

2.2 Experimental setup

The small-scale elongated pipeline gas explosion experimental platform mainly consists of the experimental pipeline, pressure acquisition system, image acquisition system, gas distribution system, and ignition system. Some of the components are shown in Figure 2.

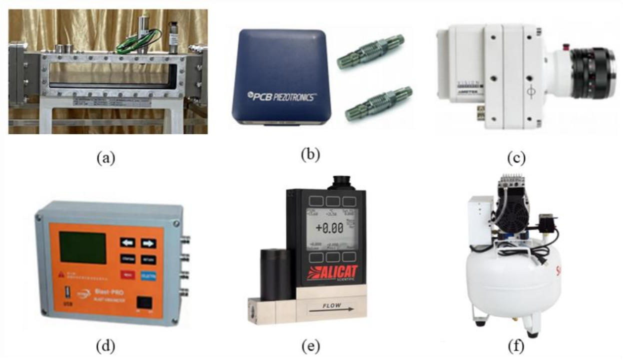

Figure 2 Experimental Equipment

(a) Experimental pipeline (with viewing window); (b) Pressure sensor; (c) High-speed camera;(d) Pressure collector; (e) Flow meter; (f) Air compressor

2.3 Experimental conditions

Before the experiment, it is necessary to check the airtightness of the pipeline and ensure that the system is functioning properly. After confirming that everything is in order, gas distribution can begin. The gas is regulated by gas flow meters to achieve the desired gas concentration, and a mixed gas equivalent to four times the volume of the experimental pipeline is continuously introduced. After the gas is introduced, both valves on the sides are closed, and the system is left to stabilize for 30 seconds to ensure uniform mixing of the premixed gas inside the pipeline. The electric igniter switch is then turned on to ignite the gas, while simultaneously collecting image and pressure data. To ensure the repeatability of the experimental results, each set of experiments is conducted at least three times.

Table 1 summarizes the experimental conditions for studying the gas explosion characteristics in utility tunnels. A 3.6m small-scale elongated gas chamber model was used as the experimental object, and the experimental design followed the requirements of GB50838-2015 standards. In this setup, air intake and exhaust vents were placed at both ends of the pipeline. Various premixed gases (with methane volume fractions ranging from 7.5% to 12.5%) were chosen to determine the methane-air concentration that had the greatest impact on the explosions. Two types of ventilation ports, bolt-sealed and thin polyvinyl chloride (PVC) film vents, were selected to investigate the effects of the number of vent openings. Additionally, obstacles were introduced into smooth pipelines with gas chamber structures (as shown in Figure 3) to study the influence of obstacle quantity. These configurations aimed to identify the methane-air concentration that had the greatest impact on the explosions and to explore the effects of the number of vent openings and obstacles on the experimental results.

Table 1 Experimental Conditions Configuration

Impact Factors	Experimental Conditions
Methane Volume Fraction	7.5%-12.5%
Number of Vent Openings	0; 1(Front); 1(Rear); 2
Number of Obstacles	0; 1; 2; 3

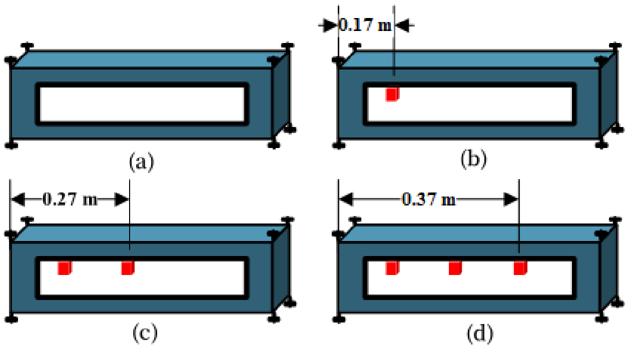

Figure 3 Schematic Diagram of Obstacle Placement

3 Results and Discussion

3.1 Influence of methane volume fraction

From the analysis of the hazards of gas explosions in utility tunnels, it is evident that the shockwave and flame front pose the greatest threat to the gas chamber. Therefore, capturing the changes in overpressure and flame propagation-related characteristic parameters during the gas explosion process becomes particularly important [20-22]. Explosion overpressure is an important indicator used to assess the consequences of gas explosion accidents [23-25]. Figure 4 shows the overpressure characteristic curves under different premixed gas concentrations. Taking 9.5% CH_4 volume fraction as an example, it can be observed from the graph that the pressure variation curve at the outlet exhibits a periodic oscillatory state, with multiple overpressure peaks occurring. This phenomenon occurs because intense chemical reactions occur in the experimental pipeline containing combustible gas after ignition, leading to rapid expansion of combustion products and acceleration of pressure wave generation. The precursor shockwave propagates forward, breaking through the PVC film at both ends to release combustion products, gradually reducing the pressure inside the pipeline and forming the first pressure peak, creating a pressure drop zone. As the flame propagates forward, the surrounding gas undergoes rapid heating, accelerating the expansion rate of combustion products beyond the venting rate of the pipeline. At this point, the pressure at the measurement point rises, creating the second overpressure peak. However, as the precursor shockwave propagates forward, it continuously attenuates due to friction with the gas and the pipe wall, resulting in excessive expansion of the explosion products and the formation of a negative pressure zone due to inertia. At this moment, the surrounding gas moves towards the center of the explosion, compressing the unburned gas again to form a flame compression wave. This wave, along with the flame propagation, accelerates the precursor shockwave. However, when the precursor shockwave hits the wall, it reflects and forms a reverse airflow, which superimposes with the flame compression wave, gradually increasing the pressure and creating the third overpressure peak. Subsequently, the precursor shockwave, accompanied by flame compression waves, oscillates back and forth multiple times at both ends of the pipeline until the maximum overpressure peak (P_{max}) is reached, gradually oscillating smaller until it approaches zero.

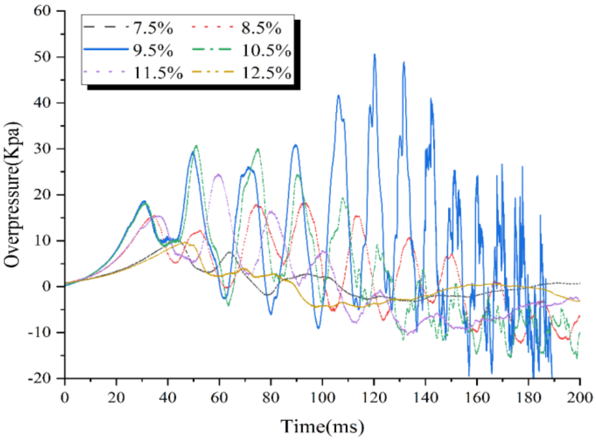

Figure 4 Overpressure Distribution under Different Methane Volume Fractions

As shown in Table 2, when the methane volume fraction is 9.5%, both P_1 and P_2 reach their maximum values. This phenomenon indicates that when the methane volume fraction approaches the stoichiometric ratio (9.5%), the severity of the gas explosion in the experimental pipeline becomes more intense. It is worth noting that the peak overpressure values at 10.5% and 11.5% are still greater than the peak overpressure value at 7.5%. This suggests that in the event of a gas explosion in an utility tunnel, higher volume fractions of natural gas leakage will result in more severe consequences. Additionally, influenced by the narrow and confined space of the utility tunnel, when an explosion occurs within the channel or pipeline, the flame propagation rate increases due to the confinement of the pipeline walls. This accelerates the stacking of precursor pressure waves along the pipeline, ultimately leading to severe pressure oscillations or even detonations. Without proper mitigation, this could result in significant destructive force [26].

Table 2 Comparison of Peak Overpressure under Different Methane Volume Fractions

Experimental Condition	Peak Overpressure P_1/kPa	Peak Overpressure P_2/kPa
7.5% CH_4	9.9425	9.8695
8.5% CH_4	16.0739	18.0850
9.5% CH_4	32.0092	48.1285
10.5% CH_4	19.8956	30.6564
11.5% CH_4	13.0647	24.3866
12.5% CH_4	7.1211	9.5695

3.2 Influence of the number of vent openings

In previous studies, it has been found that vent openings in utility tunnels can effectively reduce the structural safety risks. As concluded in Section 3.1, the explosion accident is most severe when the methane volume fraction is 9.5%. Therefore, in this section, taking a methane volume fraction of 9.5% as an example, the gas explosion characteristics under closed conditions and different venting conditions are compared and studied. Figure 5 depicts the flame propagation images of gas explosions in the second section (0.6m to 1.2 m) of the utility tunnel gas chamber model under different numbers of vent openings. It can be observed that the flame propagation of the premixed gas explosion undergoes four stages: "spherical flame - finger-shaped flame - flat flame - tulip flame". At the time from t=6ms to t=15ms, When the number of vent openings is 0 (n=0), due to the frictional force generated by the wall, there is a velocity gradient in the fluid motion. The burned gas (low-density fluid) experiences significant changes in velocity compared to the unburned gas (high-density fluid), leading to increased entrainment of unburned gas and enlarging the burning area. Consequently, the velocity difference between them increases, intensifying the flame propagation speed and deepening the concavity of the flame front inward [27]. Under the influence of buoyancy, the upper part of the flame front moves slightly faster than the lower part, resulting in a bright flame color and a mild explosive sound. When n=1(Front), the flame propagation speed is faster, and the explosion sound is louder. This is because the vent opening at the front end releases the internal gas from the opening, promoting the acceleration of flame propagation. This results in the flame front speed at the upper side being greater than that at the lower side. When n=1(Rear), the flame structure has transitioned from "Jet-Type" to "Tulip-Type". The flame propagation speed is slowest, and the flame color is brighter. The explosion sound is also louder. Different gas explosion overpressure distributions under different numbers of venting ports are shown in Figure 6. The overpressure oscillation under ventilation conditions is significantly reduced compared to closed conditions, as shown in Table 2. For the gas chamber model under different opening conditions, the reduction rates of the overpressure peaks at P1 compared to closed conditions are 47.5%, 57.7%, and 38.4%, respectively. The reduction rates of the overpressure peaks at P2 compared to closed conditions are 29.4%, 54.5%, and 35.2%, respectively. From the above data, it can be seen that compared to the closed condition, the peak overpressure values in the open conditions are significantly reduced. Additionally, due to the superposition of the compression wave, expansion wave, and shock wave at the rear end, the reduction rate of the peak overpressure at P2 is smaller than that of the peak overpressure at P1 in the corresponding conditions. Furthermore, when the number of venting ports is 1 and located far from the ignition end, the reduction rate of the pipeline's peak overpressure is the highest. Therefore, venting ports have a significant impact on the overpressure and flame effects of gas explosions in utility tunnels. The explosion hazards under open conditions are lower than those under closed conditions. According to the "Technical Code for Urban Utility Tunnel Engineering" (GB50838-2015), utility tunnels are required to have design requirements for inlet and exhaust ports. In the past, numerical simulations of gas explosions in utility tunnels mainly focused on closed, narrow-space models, leading to overestimation of the explosion characteristics. Therefore, considering factors such as inlet and exhaust ports based on the structural characteristics of utility tunnels is beneficial for accurately predicting the hazards of gas explosions in utility tunnels.

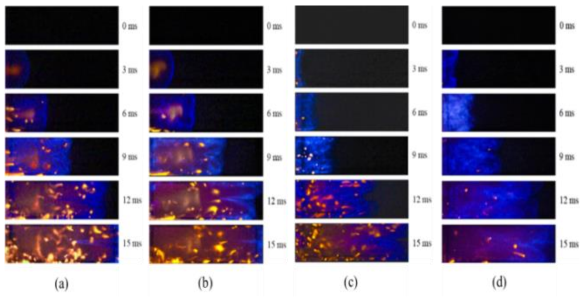

Figure 5 Flame Propagation Images with Different Venting Port Numbers

(a) n = 0, (b) n = 1 (Front), (c) n = 1 (Rear), (d) n = 2

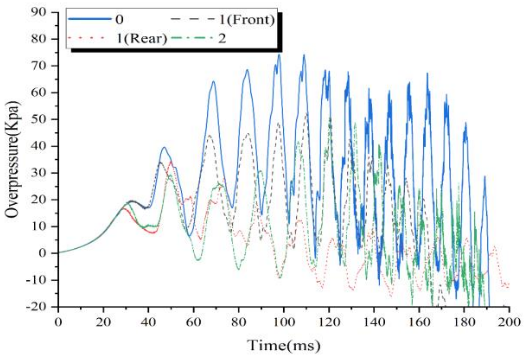

Figure 6 Pressure Distribution under Different Venting Port Numbers

Table 2 Comparison of Peak Pressure under Different Venting Port Numbers

Experimental Condition	Peak Overpressure P1/kPa	Peak Overpressure P2/kPa
n=0	48.7234	74.2330
n=1(Front)	25.5690	52.4069
n=1(Rear)	20.6287	33.7838
n=2	32.0092	48.1285

3.3 Influence of obstacle quantity

In practical engineering, the gas chambers of utility tunnels often contain equipment such as pipelines, brackets, and lighting systems, which differ significantly from other chamber spaces or tunnel structures [28]. Figure 7 shows images of flame propagation under different obstacle quantities. Compared to the smooth gas chamber model, when the obstacle quantity is 1 (o=1), the flame on the upper side is obstructed by the obstacle surface, resulting in a reduction in the flame front area and burning rate. This leads to a decrease in the propagation speed of the upper flame, with the lower flame propagating slightly faster than the upper flame. From t=9ms to t=15ms, after the flame passes through the obstacle, the folding of the flame intensifies. Under the influence of turbulent pulsations and Rayleigh-Taylor instability, the lower flame is drawn upwards, increasing the flame burning area and promoting an increase in flame propagation speed. The brightness of the flame intensifies, accompanied by an increase in the intensity of the explosion sound. When o = 2, the pattern of flame passing through the second obstacle is consistent with that of passing through the first obstacle. The flame propagation speed increases, and the growth rate shows a trend of first increasing and then decreasing. The brightness of the flame enhances significantly, appearing as an orange-yellow flame, and the explosion sound becomes particularly loud. When o = 3, the flame propagation speed and brightness decrease slightly. This is because when passing through the third obstacle, the flame propagation speed temporarily decreases due to the obstruction of the obstacle wall, resulting in a smaller flame propagation distance than the preceding case. Subsequently, as the turbulence level of the flow field increases, the flame accelerates propagation again, resulting in an orange-yellow flame and particularly loud explosion sound. It can be observed that the peak overpressure increases gradually with the increase in the number of obstacles, and the oscillation trend of the overpressure waveform becomes more pronounced. Comparing with the smooth pipeline condition, the increase rates of peak overpressure at P1 are -16.7%, 98.0%, and 176.2% respectively, while at P2, the increase rates are 127.8%, 237.6%, and 293.7% respectively. Both P1 and P2 peak overpressure values significantly increase with the increase in the number of obstacles. However, due to the proximity of sensor P1 to the obstacles and the significant superimposition of explosion waves at the tail end, the increase rate of P2 peak overpressure is greater than that of P1 in the corresponding conditions. Additionally, when o = 1, indicating a small number of obstacles, the effect of wall obstruction at the P1 measurement point in the flow field is greater than the acceleration effect of turbulence disturbance on the flame front. This leads to the opposite result in the increase rate of peak overpressure. Considering that there are many pipelines and supports in the gas chamber of the utility tunnel, it is crucial to plan the pipelines, supports, and other obstacles in the gas chamber for the safe operation of the utility tunnel.

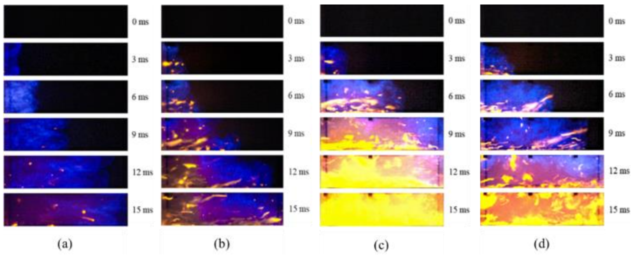

Figure 7 Flame propagation images under different obstacle quantities conditions

(a) o= 0, (b) o = 1, (c) o = 2, (d) o = 3

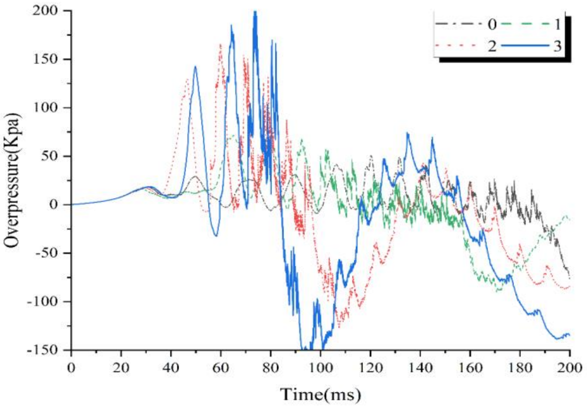

Figure 8 Overpressure characteristics curves under different obstacle quantities conditions.

Table 3 Comparison of peak overpressure values under different obstacle quantities.

Experimental Condition	Peak Overpressure P1/kPa	Peak Overpressure P2/kPa
o=0	32.0092	48.1285
o=1	26.6799	72.9017
o=2	63.3863	162.492
o=3	88.3959	189.4782

4 Conclusion

This study utilized a small-scale experimental platform based on the structural characteristics of gas chambers in utility tunnels. Through high-speed photography and pressure sensors, precise capture and collection of explosion characteristic parameters in small-scale narrow pipes were conducted. The influences of methane volume fraction, venting port quantity, and obstacle quantity on the explosion characteristic parameters of methane-air premixed gas in the pipes were analyzed. The following conclusions were drawn:

(1) As the methane volume fraction increases from 7.5% to 12.5%, the peak explosion overpressure in the experimental pipes shows a trend of initially increasing and then decreasing. When the methane volume fraction reaches 9.5%, the maximum peak overpressure generated by the gas explosion is observed. Additionally, due to the constrained space of the utility tunnel, explosions lead to an acceleration in flame propagation rate, resulting in the continuous superposition of precursor pressure waves along the pipes, ultimately leading to severe pressure oscillations or even detonations. It is necessary to implement suppression measures to ensure the safe operation of the utility tunnel.

(2) Compared to the closed conditions, the peak overpressure under ventilated conditions was reduced by up to 57.7%. At this point, the frequency of overpressure oscillations decreases, thereby reducing the overpressure damage to the tunnel structure caused by gas explosion accidents. Therefore, it is essential to regularly inspect the functionality of pressure relief devices during the operation of the utility tunnel to ensure the rapid and effective release of gases within the tunnels in the event of accidents. Additionally, during numerical simulations, considering factors such as the structure of the utility tunnel gas chamber and the presence of inlet and outlet vents would facilitate accurate prediction of the hazards posed by gas explosions in utility tunnels.

(3) The auxiliary facilities within the utility tunnel gas chamber accelerate the development of flames and also contribute to an increase in peak overpressure, amplifying the trend of overpressure oscillations, thereby leading to more significant explosion disasters. Therefore, proper planning of auxiliary facilities such as pipelines and supports within the utility tunnel gas chamber is of vital importance for the safe operation of the utility tunnel.

Acknowledgements: National Natural Science Foundation of China (NSFC 52274177, 51704054), Natural Science Foundation of Chongqing Scientific and Technological (CSTB2023NSCQ-MSX0862), Chongqing Institute of Science and Technology Master's Degree Innovation Program Project (YKJCX2220706).

References

[1]Yiping BAI, Rui ZHOU, Jiansong WU, et al.. Hazard identification and analysis of urban utility tunnels in China[J]. Tunnelling and Underground Space Technology, 2020,(103):103584.

[2]LUO Y, ALAGHBANDRAD A, GENGER T K, et al.. History and recent development of multi-purpose utility tunnels[J].

Tunnelling and Underground Space Technology, 2020,103:103511.

[3]CHEN Z-L, CHEN J-Y, LIU H, et al.. Present status and development trends of underground space in Chinese cities: Evaluation and analysis[J]. Tunnelling and Underground Space Technology, 2018(71):253-270.

[4]Jingpeng WANG. Overview of the role-playing of underground utility tunnels construction in urban development[J]. Housing & Real Estate, 2020(9):257.

[5]Hang LIU. An overview of the application of internet of things technology in the construction of urban utility tunnels[J]. Modern Information Technology, 2020,4(4):170–173.

[6]Dongwu Wang, Chunzhi DU. Experimental study on the propagation law of tunnel gas explosion[J]. Journal of Mining and Safety Engineering, 2009,26(4):475-485.

[7]Quan WANG, Ziru GUO, Zhiming LI, et al.. Experimental Study on the Propagation Characteristics of Methane-Air Premixed Flame in a Confined Tube[J]. Coal Science and Technology, 2007(11):95-97+100.

[8]Xingzhong ZHENG, Dan ZHENG. Experimental Study on the Influence of Methane Concentration and Ignition Energy on the Length of Gas Explosion Flame[J]. Fire Technology and Product Information, 2015(03):12-15.

[9]Shengguo CHEN, Yansong ZHANG, Jian LIU, et al.. Experimental Study on the Propagation Law of Natural Gas Explosion Flame and Pressure Wave in Pipeline[J]. China Safety Science Journal, 2013,9(10):43-48.

[10]HARIHARAN A, WICHMAN I S. Premixed Flame Propagation and Morphology in a Constant Volume Combustion Chamber[J]. Combustion Science and Technology, Taylor & Francis, 2014,186(8):1025–1040.

[11]Jinsheng XU, Yang LIU, Xianfeng CHEN, et al.. Influence of Methane-to-Air Mass Concentration Ratio on Flame Structure and Propagation Characteristics[J]. China Safety Science Journal, 2014,24(9):64-69.

[12]TOMLIN G, JOHNSON D M, CRONIN P, et al.. The effect of vent size and congestion in largescale vented natural gas/air explosions[J]. Journal of Loss Prevention In The Process Industries, 2015(35):169-181.

[13]MEON I. The influence of Turbulence on Flame Propagation in Obstacle Environments[C]. Montreal, Prof of First International Specialist Meeting on Fuel, Air Explosions, 1981.

[14]Barry P K. Acceleration of a flame by flame-vortex interactions[J]. Combustion And Flame, 1990(82):115-125.

[15]Jiahong JIANG, et al.. Study on the Distribution Law of Gas-Cloud Explosion Field in Urban Comprehensive Pipe Gallery[D]. Nanjing: Nanjing University of Science and Technology, 2018.

[16]XU Y, HUANG Y, LI J, et al.. A risk-based optimal pressure relief opening design for gas explosions in underground utility tunnels[J]. Tunnelling and Underground Space Technology, 2021(116):104091.

[17]WANG S, LI Z, FANG Q, et al.. Numerical simulation of overpressure loads generated by gas explosions in utility tunnels[J]. Process Safety and Environmental Protection, 2022(161):100-117.

[18]Xinsheng JIANG, Wei XIE, Yadong ZHAO, et al.. Experimental Study on Oil and Gas Explosion in Long and Narrow Pipelines with Different Length-to-Diameter Ratios[J]. Oil & Gas Storage and Transportation, 2020,39(8): 879-884.

[19]Zhenmin LUO, Jing SHI, Tao WANG, et al.. Study on the Influence of NH_3 on CH_4 Explosion Characteristics and Reaction Kinetics[J]. Journal of Safety Science and Technology, China, 2020,30(9):51-58.

[20]L PANG, T WANG, Q ZHANG, et al.. Nonlinear distribution characteristics of flame regions from methane–air explosions in coal tunnels[J]. Process Safety and Environmental Protection, 2014(92):193-198.

[21]J WEERHEIJM, J VERREAULT, M. VAN DER VOORT, et al.. Quantitative risk analysis of gas explosions in tunnels[J]. Fire Safety Journal, 2018(97):146-158.

[22]L WANG, H MA, Z SHEN, et al.. A comparative study of the explosion behaviors of H2 and C2H4 with air, N2O and O2[J]. Fire Safety Journal, 2021(119):103260.

[23]LIY C, BI M S, ZHOU Y H, et al.. Experimental and theoretical evaluation of hydrogen cloud explosion with built-in obstacles[J]. International Journal of Hydrogen Energy, 2020,45(51):28007-28018.

[24]GUO C W, JIANG S G, SHAO H, et al.. Suppression effect and mechanism of fly ash on gas explosions[J]. Journal of Loss Prevention in the Process Industries, 2022(74):104643.

[25]WANG Q H, SUN Y L, JIANG J C, et al.. Inhibiting effects of gas-particle mixtures containing CO2, Mg(OH)2 particles, and NH4H2PO4 particles on methane explosion in a 20-L closed vessel[J]. Journal of Loss Prevention in the Process Industries, 2020(645):104082.

[26]DU Y,ZHANG P L,ZHOU Y,et al.. Suppressions of gasoline-air mixture explosion by non-premixed nitrogen in a closed tunnel[J]. Journal of Loss Prevention in the Process Industries, 2014(31):113-120.

[27]Tingxi XU, Xuede WANG, Xiaobo ZHANG, et al.. Numerical Study on the Influence of Air Intake Position on Inerting Characteristics of Fuel Tanks[J]. Aeronautical Computing Technique, 2015,45(4):105–108.

[28]Shuwang WEI, Xinsheng JIANG, Biao HE, et al.. Experimental Study on the Inhibition of Oil and Gas Explosions in Narrow and Confined Spaces by C_3HF_7 [J]. China Safety Science Journal, 2016,12(7):128–133.

Viser Technology Pte. Ltd.
Research and Application of Materials Science
DOI: 10.33142/rams.v5i2.12707

Research Article Open Access

Study on the Effects of Helium-Argon Gas Mixture on the Laser Welding Performance of High Temperature Alloys

Xiongzi CHEN [1, 4], Hesi PENG [2], Chunchen YAO [1, 3*], Yu DAI [1, 4], Yewen QIN [2]

1. Hunan Dingli Technology Co., Ltd., Changsha, Hunan 410137, China
2. Changsha Tianchen Laser Technology Co., Ltd., Changsha, Hunan 410100, China
3. Jiangnan Industrial Group Co., Ltd., Xiangtan, Hunan 411207, China
4. School of Materials Science and Engineering, Nanchang University, Nanchang, Jiangxi, 330031, China

**Corresponding author:* *Chunchen YAO, E-mail: yaocc112@163.com*

Abstract

In order to solve the problem of porosity in laser deep penetration welding of GH3625 high-temperature alloy plates, five different ratios of high-purity helium gas and high-purity argon gas mixed gases were compared in welding experiments after various process parameter improvements and adjustments failed to achieve Class I welds. The experimental results show that using high-purity helium gas or a mixture of 50% high-purity helium gas and 50% high-purity argon gas can both achieve Class I welds. This indicates that using high-purity helium gas or an appropriate mixed gas instead of pure argon is one of the effective ways to solve the problem of porosity in laser deep penetration welding of high-temperature alloys. The mixture of 50% high-purity argon gas and 50% high-purity helium gas can reduce the consumption of high-purity helium gas, lower production costs, and is more suitable.

Keywords: *high-temperature alloy; laser welding; pores; shielding gas; welding quality*

1 Introduction

With the progress of science and technology and the development of economic construction, the application of high-temperature alloys in aerospace, energy, and chemical industries has become increasingly widespread. A GH3625 high-temperature alloy part whose welding quality is affected by the presence of weld porosity in the weld test plate. Despite measures such as strengthening pre-weld cleaning and optimizing welding process parameters, the porosity problem remains unresolved, and the weld does not meet the requirements of a Class I weld. In order to solve the porosity problem in laser deep penetration welding of GH3625 alloy, comparative welding experiments were conducted on GH3625 alloy plates using helium-argon mixed gas with different ratios.

During laser deep penetration welding, a laser beam with a power density of 10^7 W/cm^2 or higher can vaporize the metal in the heating zone in a very short time, forming a small hole in the liquid molten pool, which is called a keyhole [1]. The mechanism of pore formation is the formation of bubbles in the closed space after the collapse of the keyhole, and the bubbles are not able to escape from the surface of the molten pool and are captured by the solidification interface [2]. Laser deep penetration welding of metal materials such as steel and aluminum alloys is prone to pore formation, and high-temperature alloys with high contents of alloying elements such as Ni and Mo have poor fluidity of the molten pool during laser welding, making it difficult for gases in the molten pool to escape, resulting in a higher tendency for pore formation.

Xiao Rongshi et al. [3-4] applied the method of using a mixture of argon and helium as a protective gas in CO_2 laser deep penetration welding. Through comparative experiments, it was found that when using pure argon as the shielding gas, plasma shielding phenomenon occurs at around 5KW laser power, but the plasma shielding phenomenon disappears after adding helium. Lei Zhenglong et al. [5] found that when pure helium is used as the protective gas in aluminum alloy laser self-melting welding, it has a significant effect on suppressing pores, enhancing pore stability, and reducing the porosity to below 1%. He Shuang [6] found that adding helium to the protective gas during A7N01 aluminum alloy laser-MIG hybrid welding can enhance the stability of the welding process and avoid the instability of the pores, thus preventing the formation of weld porosity. As the proportion of helium in the helium-argon mixed shielding gas increases, the porosity of the weld

Received on October 27, 2023; Accepted on November 30, 2023

gradually decreases. After the helium content reaches 50%, the porosity of the weld does not change significantly, and it is reduced by about 80% compared with high-purity argon. Su Xiaoyang et al. [7] found that in helium-argon mixed protective gas laser + arc hybrid welding, when the volume fraction of helium in the protective gas increases to 5% and 10%, the arc pressure and electric potential gradient increase, and the weld penetration depth also increases.

Through literature research, it has been found that helium-argon binary shielding gas is superior to pure argon shielding gas in laser welding process in terms of pore suppression, weld penetration depth, joint quality, etc. Moreover, there are already studies proving that a mixed shielding gas of helium (50%) and argon (50%) has the best effect on pore suppression in laser melting welding of aluminum alloys. Currently, there is little research on porosity suppression in laser welding of high-temperature alloys, and the use of helium-argon binary gas as a shielding gas has not been reported. Key parameters such as gas flow rate, mixing ratio, and porosity rate still need to be experimentally verified.

2 The Problem of Pores in Laser Welding of GH3625 Alloy Plate

After laser welding, there are no cracks or pores found in the appearance inspection of GH3625 high-temperature alloy plates with thicknesses of 2 mm and 3 mm. However, when the weld seam is cut open and polished for microscopic examination, internal pores on the cross-section of the weld seam can be easily observed. Figure 1 shows the internal pores on the cross-section of the weld seam of the 2 mm thick welding specimen, located in the lower part of the weld seam.

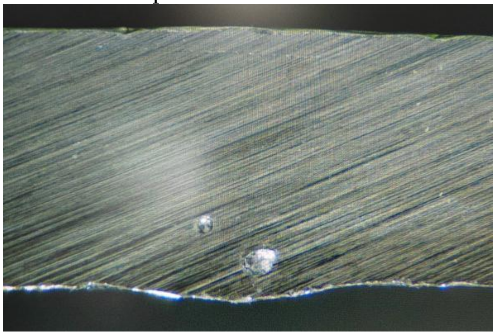

Figure 1 Pores inside the weld seam of the 2 mm specimen (15×)

If X-ray testing is performed on the welded test plate, it can be found that there are many pores in the weld, which does not meet the requirements of the weld grade. When a tensile test is conducted on the sample, the strength of the welded joint does not meet the quality requirements. Figure 2 shows a group of pores on the fracture surface of the unqualified sample with a thickness of 2 mm. The pores are densely distributed in the lower part of the weld.

Figure 2 Group of pores on the fracture surface of the unqualified tensile sample (5×)

In order to solve the problem of porosity in GH 3625 alloy plate laser welding, a lot of work has been done in the pre-weld cleaning and optimization of welding process parameters of the test plate. Although there has been progress, the weld has not been able to meet the quality requirements of Grade I. Therefore, we are looking for solutions to the porosity problem from the aspect of shielding gas.

3 Comparative Experiment of Laser Welding with Different Ratios of Helium-Argon Gas Mixture

In order to gain a deeper understanding of the effects of argon gas, helium gas, and argon-helium gas mixture on laser welding, it was decided to conduct a comparative experiment on laser welding of GH3625 alloy plates using five different gas ratios.

3.1 Pre-welding preparation

3.1.1 Welding equipment

The welding equipment used the 2000W laser welding experimental platform from Changsha Tianchen Laser. It includes a 3-axis precision welding platform, a Chuangxin 2000 laser, a Jizhi Mechanical and Electrical 3000 water cooler, and a Hanwei dual swing laser head.

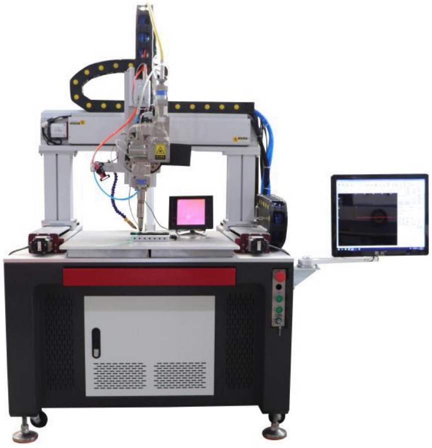

Figure 3 2000W Laser Welding Experimental Platform

3.1.2 Welding test plate

Two pieces of GH3625 high-temperature alloy plates with a thickness of 2 mm were used. Each test plate is approximately 150 mm long and 120 mm wide. The material of the test plate has undergone acceptance inspection, and its chemical composition meets the requirements of GB/T 14992 [8].

3.1.3 Protective gas

Bottled high-purity argon gas and bottled high-purity helium gas were used. Both gases have qualified certificates after inspection.

3.2 Welding experiment

Laser welding was performed using 5 different gas ratios. During welding, only a single test plate was melted, and butt welding was not performed temporarily. The gas ratio was controlled by flow adjustment. Three welds were made for each gas ratio. Before each weld, the welding area was carefully cleaned with alcohol and dried with a hairdryer. A total of 15 welds were made, using up both test plates. The welding sequence, gas ratio, and welding power are shown in Table 1.

Table 1 Gas Composition and Welding Power of Comparative Experiments

Serial Number	Gas Composition and Flow Rate	Weld Seam Number	Welding Power (W)
1	100% High Purity Argon Gas, 25L/min	1	700
		2	760
		3	760
2	75% High Purity Argon Gas, 21L/min +25% High Purity Helium Gas, 7L/min	4	760
		5	760
		6	760
3	50% High Purity Argon Gas, 14L/min +50% High Purity Helium Gas, 14L/min	7	760
		8	760
		9	760
4	25% High Purity Argon Gas, 21L/min +75% High Purity Helium Gas, 7L/min	10	760
		11	760
		12	760
5	100% High Purity Helium Gas, 25L/min	13	760
		14	760
		15	760

3.3 Test results

The results of the above 15 welds, which were subjected to X-ray inspection ratings, are shown in Table 2.

From Table 2, it can be seen that when the helium content reaches 50% or more, it can effectively reduce the quality of pores and improve the weld grade. This is mainly because the basic physical properties of argon gas and helium gas are shown in Table 3. The atomic mass of argon gas is about ten times that of helium gas, and the relative air density is ten times that of helium gas, which means that argon gas has a higher gas density and the low-density helium gas is more likely to escape after entering the molten pool, reducing the porosity of the weld. At the same time, the thermal conductivity of argon gas is small, about one-tenth that of helium gas, which means that helium gas is more capable of conducting heat and has less impact on laser energy, making the welding process more stable compared to argon gas. On the other hand, the first ionization energy of argon gas is 15.75 eV, while the first ionization energy of helium gas is 24.58 eV. Helium gas has the lowest ionization energy and can quickly remove the rising metal vapor generated from the molten pool. Using helium as a protective gas can effectively suppress plasma and reduce the formation of pores. However, due to its higher price, considering cost reduction and the actual welding results, a gas ratio of 50% high-purity argon gas and 50% high-purity helium gas is the most suitable for protection.

Table 2 X-ray detection results of comparative experiments with different gas ratios

Serial Number	Gas ratio for protection	Weld Seam Number	X-ray detection rating
1	100% high-purity argon gas	1	II
		2	II
		3	II
2	75% high-purity argon gas + 25% high-purity helium gas	4	II
		5	II
		6	II
3	50% high-purity argon gas + 50% high-purity helium gas	7	I
		8	I
		9	I
4	25% high-purity argon gas + 75% high-purity helium gas	10	I
		11	I
		12	I
5	100% high-purity helium gas	13	I
		14	I
		15	I

Note: Rating standard NB/T 47013.2-2015 [9].

Table 3 Comparison of Physical Properties of Helium and Argon Gases

Gas	Boiling Point (1.013bar)(℃)	Atomic Mass (Kg/Kmol)	Density (0℃1.013bar)(Kg/m^3)	Relative Density Of Air (0℃1.013bar)	Thermal Conductivity(W/Mk)
Ar	-185.9	39.948	1.784	1.380	0.017
He	-268.9	4.002	0.178	0.138	0.154

4 Production Application

By using improved shielding gas and other methods, the 2mm and 3mm GH3625 alloy butt-welded test plates achieved Class I welds. The test plates were sampled and tested for mechanical properties, which passed the expert evaluation and were applied to the welding production of GH3625 components.

5 Discussion

5.1 Using high-purity helium gas or a suitable mixture of helium and argon gases can significantly reduce the generation of pores

From the comparative test of helium-argon gas in this study, it can be concluded that replacing pure argon with high-purity helium gas or a mixture of 50% high-purity argon gas and 50% high-purity helium gas can significantly reduce the generation of pores. This is one of the ways to solve the problem of porosity in laser deep penetration welding of GH3625 high-temperature alloy.

5.2 The advantages of using a 50% high-purity argon gas + 50% high-purity helium gas mixture

Due to the high cost of high-purity helium gas and the higher production cost, using a 50% high-purity argon gas + 50% high-purity helium gas mixture can achieve the same effect as using high-purity helium gas, while reducing the consumption of high-purity helium gas and lowering the production cost. Therefore, using a 50% high-purity argon gas + 50% high-purity helium gas mixture is more suitable.

6 Conclusion

Replacing pure argon with high-purity helium gas or a 50% high-purity argon gas + 50% high-purity helium gas mixture can significantly reduce the formation of gas pores in laser deep penetration welding of GH 3625 high-temperature alloy plates with thicknesses of 2 mm and 3 mm. It is an effective way to solve the problem of gas pores in laser deep penetration welding of high-temperature alloys.

By using a mixture of 50% high-purity argon gas and 50% high-purity helium gas, the consumption of high-purity helium gas can be reduced, and the production cost can be lowered.

Other experts and technicians who participated in this test work include Wu Zhiqiang and Fang Minpark of Changsha Tianchen Laser Technology Co., Ltd, Mei Boazhan, Xie Huipeng and Qiu Congzhang of Hunan Toplite Technology Co., Ltd, Cao Zhi and Hao Xingxing of CU Intelligent Technology Co. We would like to express our heartfelt thanks to all the participants and supporters of this experiment!

Acknowledgements: Project of Tian chi talent leader in Xinjiang Uygur Autonomous Region (2022).

References

[1]Chen Yanbin. Modern Laser Welding Technology[M]. Beijing: Science Press, 2005.

[2]Huang Lijin, Liu Peng, Zhu Su, et al.. Numerical Simulation of Gas Pores in Aluminum Alloy Laser Welding[J]. Shipbuilding Technology, 2020(2):1-6,12.

[3]Xiao Rongshi, Zuo Tiechuan. Study on the Control of CO2 Laser Deep Penetration Welding Plasma [J]. Chinese Journal of Lasers, 1997,24(5):461-466.

[4]Xiao Rongshi, Mei Hanhua, Zuo Tiechuan. Influence of Auxiliary Gas on the Shielding of CO2 Laser Welding Plasma [J]. Chinese Journal of Lasers, 1998,11(11):1045-1050.

[5]Lei Zhenglong, Li Ying, Chen Yanbin, et al.. Influence of dual-beam laser wire filling welding process on porosity of aluminum alloy welds [J]. Welding Journal, 2013,34(2):40-44.

[6]He Shuang. Influence of helium-argon mixed shielding gas on the characteristics of laser-MIG hybrid welding of A7N01 aluminum alloy [D]. Southwest Jiaotong University, 2018.

[7]Su Xiaoyang, Liu Wen, Xu Guoxiang, et al.. Numerical analysis of arc characteristics in helium-argon mixed shielding gas rotary laser + arc hybrid welding of butt joints [J]. Journal of Precision Forming Engineering, 2023,15(4):164-175.

[8]GB/T14992-2005. Classification and Grades of High-Temperature Alloys and Intermetallic Compounds[S]. Beijing: China Standard Press, 2005.

[9]NB/T 47013.2-2015. nondestructive testing of pressurized equipment Part2:Radiographic testing[S]. Beijing: Xinhua Publishing House, 2015.

Viser Technology Pte. Ltd.
Research and Application of Materials Science
DOI: 10.33142/rams.v5i2.12708

Research Article Open Access

Development and Application of Modern Building Ceramic Materials

Chaolu YANG[1†], Fuchuan ZHOU[2*], Qianren CHEN[1†], Gang SHI[3], Masiko M. Kaziana [2, 4], Masabo Gasper[2, 4]

1. Institute of New Manufacturing Engineering, Tomsk Polytechnic University, Tomsk, 634050, Russia
2. Chongqing Vocational Institute of Engineering, Chongqing, 402260, China
3. Chongqing yuxi water conservancy and electric power survey and design institute CO., LTD., Chongqing, 402160, China
4. Dar es Salaam Institute of Technology {DIT}, Dar es Salaam, 11103, Tanzania

[*]***Corresponding Author:*** *Fuchuan ZHOU, E-mail: 981480645@qq.com*

Abstract

With the increasing demand for sustainable building design, modern building ceramic materials are one of the key factors driving innovation and development in the field of architecture, thanks to their excellent performance and environmentally friendly properties. The aim of this study is to provide an insight into the development and application of building ceramic materials in modern architecture, and to assess the contribution of material innovation to architectural design and sustainability goals by synthesising and analysing recent technological advances and case studies in this field. This study adopts a systematic literature review approach to screen and analyse a large number of academic articles and practical project reports on material innovation in building ceramics. Comparative analyses of different material properties, advances in production processes and the effects of their application in real building projects reveal the potential of building ceramic materials to improve the energy efficiency, extend the service life and enhance the aesthetic design of buildings. The findings show that the environmental and energy issues facing traditional building materials, such as improved thermal efficiency and a reduction in the overall carbon footprint of buildings, can be effectively addressed through the use of new building ceramic materials and technologies. In addition, the innovative use of architectural ceramics provides architects with more design flexibility, enabling them to create architectural works that are both aesthetically pleasing and functional. In the concluding section, the paper highlights the importance of continuing to explore technological innovations in building ceramic materials and how these innovations can contribute to a more sustainable and environmentally friendly building industry. Future research should further explore new areas of application for ceramic materials and how interdisciplinary collaboration can accelerate the practical application of these material technologies.

Keywords: *ceramic materials; sustainability; modern architecture; development and applications*

1 Introduction

In the long history, the development of building materials has always been an important force to promote the progress of architectural art and science. From mud bricks and wood in ancient times to steel and concrete in modern times, each material innovation has brought about changes in the way buildings are designed and constructed [1]. In the 21st century, this process has reached new milestones, especially in the field of architectural ceramic materials. In the last decades, modern building ceramic materials have undergone remarkable technological innovations and application expansions [2]. The building ceramic materials of recent years have not only achieved significant advances in performance and functionality, but have also demonstrated great potential for environmental protection and digitalisation.

In recent years, with the advancement of materials science, especially nanotechnology [3] and intelligent manufacturing technology [4-5], architectural ceramic materials are no longer limited to traditional decorative and structural uses only. The convergence of these technologies has resulted in modern ceramic materials with additional functionalities such as self-cleaning capabilities [6], improved thermal [7-8] and acoustic isolation properties [9], and even enhanced flexibility and transparency. The enhancement of these attributes has greatly enriched architects' design toolbox [10], providing

Received on October 13, 2023; Accepted on November 29, 2023

them with unprecedented creative freedom and room for expression [11].Furthermore, environmental sustainability has taken centre stage in the development of building materials in recent years [12]. The production and application of modern building ceramic materials increasingly takes into account the need to save energy and reduce environmental impact. This not only includes optimising production processes to reduce waste and emissions, but also involves the development of recyclable or biodegradable [13] ceramic materials. These endeavours open up new possibilities for material innovation and diversity while pushing the construction industry towards green sustainability. The application of digital technologies, especially 3D printing [14-15], has played an important role in the innovation of modern building ceramic materials. These technologies have not only allowed ceramic materials to be made in more diverse shapes and sizes, but have also improved the precision and efficiency of manufacturing. Through these technologies, designers are able to realise more complex and fine architectural details, further pushing the boundaries of architectural design.

In this paper, we will explore in depth how the latest scientific research and technological breakthroughs have enabled a quantum leap in the use of modern ceramic materials in architecture. We will focus on how these advances have influenced the way architectural design is thought of, and how they are helping to realise a more efficient, environmentally friendly and aesthetically pleasing built environment. We will also explore new directions for the future development of building materials technology.

2 Literature Review

2.1 History of the development of ceramic materials

In the traditional sense, a ceramic is any of a variety of hard, brittle, heat- and corrosion-resistant materials made by moulding and firing inorganic non-metallic materials, such as clay, at high temperatures [16-17].Common examples are pottery, porcelain and brick. Traces of ceramics can be found as far back as the beginning of human history. The first ceramics made by humans were brick walls used to build houses and other structures, while pottery (jars, vessels, or vases) or figurines made of clay, either alone or mixed with other materials (such as silica), hardened and sintered in a fire was a common practice in the production of ceramics. Later, ceramics were glazed as well as fired to produce smooth, coloured surfaces, and porosity was reduced by using glassy, amorphous ceramic coatings on top of crystalline ceramic substrates [18]. Ceramics now include household, industrial and architectural products, as well as a variety of materials developed for advanced ceramic engineering, such as semiconductors. In the process of this change, the concept of ceramics has gradually changed from the traditional pottery, stoneware, porcelain and bone china made from clay-based materials to the more generalised ceramic matrix composites.

2.2 Types and properties of building ceramics

2.2.1 Oxide ceramics

Typically, the raw materials for modern ceramics no longer include clay [19].Modern ceramics are mainly classified in three different materials: firstly, oxides, common examples of which are aluminium oxide, beryllium, cerium oxide and zirconium oxide, are made by a series of methods such as sintering and pressing; such ceramics usually have a high melting temperature as structural materials, and are very stable in oxidising atmospheres. With the exception of beryllium oxide ceramics, their thermal conductivity is low. They are usually dosed with ultrafine powders and small amounts of sintering accelerators and modifying additives. The atomic bonding of oxide ceramic materials is dominated by ionic bonding, with some covalent bonding present, so they have many excellent properties. Most of the oxides have high melting points, good electrical insulation properties, especially excellent chemical stability and oxidation resistance, and have been more widely used in the engineering field [20].Such ceramics can continue to be subdivided by component for single oxide ceramics, as well as composite oxide ceramics are different from traditional ceramic materials for daily use, high-tech oxide ceramic materials special electric, magnetic, optical, thermal, acoustic, chemical, biological, piezoelectric, thermoelectric, electro-optical, acousto-optic and magnetic properties, are classified as high-performance structural and functional ceramics. In the construction industry, these materials are mainly used in applications that require high wear and corrosion resistance or are subjected to high-temperature environments. For example, aluminium oxide (Al_2O_3) ceramics with high weather resistance and colour stability are used as building facade materials to provide long-term appearance retention and protection [21].

2.2.2 Non-oxide ceramics

The second type of ceramics is the non-oxide ceramics represented by carbides, borides, nitrides, silicides and so on. It as a non-oxide system of high temperature resistant structural materials, carbon silicon carbide, silicon nitride, aluminium nitride and other materials and the plug complex silicon nitride solid solution as raw materials. Therefore, non-oxide high temperature ceramics have excellent high temperature strength, low coefficient of thermal expansion, close to the thermal conductivity of the metal, resistance to oxidation, resistance to corrosion of high sulphur fuels, resistance to external stress and thermal shock and other characteristics. Non-oxide ceramics differ from oxide ceramics in a number of ways. Firstly, due to the scarcity of non-oxide in nature, usually less than 1% in the earth's crust, most of the raw materials need to be artificially refined and synthesised. Secondly, from the Gibbs thermodynamic function, we can learn that the standard free enthalpy of generation of non-oxide ΔG is generally greater than the corresponding standard free enthalpy of generation of oxide ΔG. This phenomenon is closely related to the high electronegativity of oxygen and the ability to form stable chemical bonds. The chemical bonding between oxide atoms is mainly ionic bonding, while non-oxides are generally covalent bonds with strong bonding. The above differences result in non-oxide ceramics being more difficult to sinter than oxide ceramics. Because the standard free enthalpy of generation of non-oxide ΔG is greater, non-oxide ceramics in the synthesis of raw materials and ceramic sintering, easy to generate oxides, and therefore must be carried out in a protective gas (such as N2, Ar, etc.). The raw materials of oxide ceramics are themselves oxides, so there is no fear of oxidation, so the production process is relatively simple.

Although non-oxide ceramics are difficult to sinter, it is also one of their major advantages. Non-oxide ceramic materials, due to the predominantly covalent bonding in their atomic structure, exhibit excellent physical and chemical properties. The high hardness, modulus of elasticity and creep resistance of these materials, and the stability of their properties especially at elevated temperatures, provide ideal conditions for their use in extreme environments. These attributes, a significant advantage over traditional oxide ceramic materials, make non-oxide ceramics ideal for use in fields such as aerospace, automotive manufacturing, and electronics. However, the widespread use of non-oxide ceramics does suffer from a number of constraints, one of which is their own brittleness and the challenges they face when joining with other materials such as metals. Nonetheless, the applications of these high-temperature structural materials remain promising, and researchers are addressing these issues through various approaches, such as interface engineering, design of functional gradient materials, and the use of advanced ceramic matrix composite technologies to enhance connection strength and durability. In building materials, high-strength and high-hardness non-oxide ceramics, such as silicon carbide, can be used as decorative or protective building materials for special structural applications. For example, as a protective layer for the outer shell of a building to enhance durability and corrosion resistance. Their excellent resistance to high temperatures also allows non-oxide ceramics to be used in parts of the interior of buildings that require refractory materials, such as chimney linings, fireplaces, boiler rooms and high-temperature furnace linings. And in areas that need to be very hard-wearing, such as commercial spaces, industrial plants or car parks, non-oxide ceramic materials can be used as floor cladding materials to provide a durable surface. In addition, there are many other potential or actual applications for non-oxide ceramics in the construction sector, which are not as commonly used as other building materials, but still have a promising future.

2.2.3 Composite ceramics

The third category of ceramics is ceramics made from composite materials, and ceramic matrix composites. Ceramic composites are a class of materials made from a combination of at least two different materials, at least one of which is a ceramic. Ceramics are often chosen for their good thermal stability, chemical resistance and high hardness, but they are also prone to brittle fracture. By combining them with other materials, their mechanical properties, such as increased toughness and fracture resistance, can be significantly improved, making them more suitable for a variety of engineering applications. There are a wide range of types and uses for ceramic composites, and several common ceramic composites and their properties are described in detail below: Particle-reinforced ceramic composites, which enhance the mechanical properties of the composite by adding hard particles (such as silicon carbide (SiC) particles) to the base ceramic (such as aluminium oxide (Al_2O_3)). The addition of particles can improve the hardness and wear resistance of the composites. However, the distribution, size and volume fraction of the particles must be carefully controlled to avoid excessive weakening of the material's toughness: fibre-reinforced ceramic composites, which improve the toughness and fracture resistance of the material by embedding continuous or short fibres in the ceramic matrix. Commonly used reinforcing fibres include carbon fibres and ceramic fibres (e.g. silicon carbide fibres). These fibres effectively transfer stresses and bridge cracks when force is applied, thus improving the overall performance of the material. As well as layered ceramic composites, they usually consist of alternating layers of different materials, each with a specific function. For example, one layer may have a high hardness to provide wear resistance, while another layer may have a higher toughness to absorb energy and stop crack propagation. Composites with this structure are particularly useful in wear-resistant and protective applications: there are also self-healing ceramic composites, which contain specific components that respond to damage within the material. When a crack occurs, these components react chemically, filling the crack and restoring some degree of material integrity. This type of composite is particularly valuable for increasing long-term reliability and reducing maintenance costs.

In the construction sector, ceramic composites are used in many high-performance application scenarios due to their unique properties. For example, they are used in facade and curtain wall systems. Ceramic composites can be used as curtain wall systems on the exterior of buildings due to their abrasion and corrosion resistance. These materials not only provide an aesthetically pleasing and modern look to a building's exterior, but can also withstand harsh environmental conditions, including temperature changes, UV exposure and the effects of chemicals. Traditional roof tiles can also be made from ceramic composites to improve their durability and functionality. For example, solar cells can be embedded in roof tiles for energy harvesting and use.As well as floor and wall tiles by adding specific composite materials to improve hardness and wear resistance. Ceramic composite floor tiles with the addition of, for example, silicon carbide, alumina or diamond particles can withstand higher friction and pressure. There are also a range of areas of construction engineering where ceramic composites can be used, such as bridges and infrastructure, earthquake-resistant components, decorative panels and acoustic materials.

In summary, the use of ceramic composites can improve the durability of buildings, reduce maintenance costs, enhance functional performance, and enhance the aesthetic and environmental performance of buildings. With technological advances and material innovation, it is expected that ceramic composites will play a more important role in the construction industry in the future.

3 The Development of Modern Building Ceramics Technology

Modern building ceramics technology has undergone significant development and innovation. Today, building ceramics is not just a decorative material in the traditional sense, but an advanced building material that integrates aesthetics, functionality and durability. From the basic materials, traditional ceramic materials such as porcelain clay, glaze after reformulation and modification, its physical strength and durability has been significantly improved. At the same time, the development of new materials such as lightweight ceramics, high-performance oxide ceramics and ceramic composites has greatly improved the functionality of building ceramics, such as enhanced thermal and acoustic insulation, weathering and self-cleaning functions. And from the technical side, intelligent manufacturing technology, green sustainable technology, intelligent ceramic technology and surface treatment technology have all made great progress in recent years.

3.1 Intelligent manufacturing technology of ceramics

3.1.1 Ceramics intelligent manufacturing technology of the main research direction

Modern building ceramics intelligent manufacturing technology, mainly embodied in two aspects, one is to computer-aided design (CAD) as the representative of the digital design technology, on the other hand, is embodied in the inclusion of three-dimensional printing (3D Printing), computer numerical control (CNC) machining, as well as automation and robotics systems on the digital production technology. Take 3D Printing technology as an example, since the United States Hull in 1986 for the first time proposed [22] three-dimensional light-curing technology (SL), digital light processing technology (DLP), as well as two-photon polymerisation technology (TPP) also appeared one after another. The above methods usually use organics ceramic precursors (preceramic polymers, PCPs) photosensitively polymerisable liquid systems or slurry systems containing a mixture of photosensitive solutions and ceramic powders. Photosensitive polymerisation, i.e., light curing, refers to a certain volume of liquid materials such as polymer monomers that are irradiated by light at a certain wavelength to cause cross-linking polymerisation reactions to complete curing [23]. In terms of this 3D printing process, it is actually the resin polymerisation crosslinking into a mesh structure uniformly wrapping the ceramic particles dispersed in the system, thus macroscopically forming the curing of the mixed material. Afterwards, the printed parts are subjected to high-temperature degreasing and sintering processes and the organic matter in the samples is discharged, the ceramic samples are further densified, and at the same time the grains are enlarged to form the final samples, which is similar to the traditional ceramic fabrication methods in this heat treatment stage. PCPs can be photosensitive polymerisation of liquid systems is more through chemical changes, which is similar to the ordinary photosensitive resin light-curing 3D printing process, followed by high-temperature pyrolytic ceramisation to become the required precursor conversion ceramics (polymer derived ceramics, PDCs) samples.

Stereolithography (SL) is a popular 3D printing technology that is now widely used. During the printing process, a beam of specific wavelength (usually UV light) is usually used to scan and cure the surface of the material system in point-line-face scanning, followed by layer-by-layer stacking, and progressive construction from the longitudinal direction; when a layer is cured, the construction of the next layer is started by elevating or decreasing the thickness of one layer. Digital light processing (DLP) is a technology that can produce high surface quality parts with micron resolution because of the extremely fine spot size of its beam (60-140 μm).

Digital light processing, on the other hand, is actually a mask-based surface-exposure SL technology. This technology exposes a whole layer of printed shapes after layering to the photosensitive resin surface for layer-by-layer curing through a light source in a single pass through a mask. The concept was initially realised by Nakamoto and Yamaguchi in Japan in 1996 through the use of a solid mask [24].In 1997, it was further improved by Bertsch et al. using a liquid crystal display (LCD) as a dynamic mask generator [25]. Since 2001, Texas Instruments' digital mirror device (DMD) has dramatically improved the display resolution and contrast due to its competitive fill factor and reflectivity, subsequently replacing LCD as a new generation of mask technology for use in DLP printing [26].The DMD is made up of millions of display image pixels corresponding to the DMD is a chip composed of a rectangular array of micromirrors corresponding to the pixels of the displayed image. The micromirrors are driven by electrostatic force and can be individually rotated ±(10~12)°to serve to control the state of ultrafast light on or off. In this way, an incident light beam with a spatial resolution of 1.1 μm is reflected across or deflected away from the lens, causing the pixels to appear light or dark on the projection surface [27]. Ultra-fast light switching and overall projection allow DLP 3D printing processing times to be significantly shorter than conventional SL point-line-plane scanning processes, and micron-level feature resolution can be achieved, enabling parts to be fabricated more quickly and with higher accuracy [28].

3.1.2 Problems and challenges of ceramic sl and dlp processes

The ceramic SL and DLP process mainly uses ceramic light-curing slurry made by mixing ceramic powder and photosensitive solution. This approach is more or less faced with a number of problems and challenges, such as ceramic raw material powder particle size distribution and morphology is not ideal, slurry precipitation, viscosity is too large, 3D printers need to add a scraper for slurry scraping level, hindering the further development of ceramic 3D printing technology. The above problems can be effectively solved by the clever combination of organic precursor ceramic conversion (PDC) technology, which is different from ceramic powder-photosensitive solution, and 3D printing.PDC technology is a polymer that can be converted into ceramic material by heat treatment by chemical method, and pyrolysis can be converted into precursor ceramics within a certain range of temperatures [23]. Precursor polymers control the composition and microstructure of precursors through molecular design, and the presence of chemically reactive groups undergoes cross-linking, which results in higher yields of ceramics that are pyrolysed after cross-linking [23]. Preparation of ceramic materials by pyrolysis of organic ceramic precursors (PCP) is a new method developed in recent years for the preparation of ceramic materials and components, the technology has the characteristics of simple processing, precursors are easy to isolate and purify, inherited the excellent moulding properties of polymer materials and high-temperature stability of ceramic materials, so that the traditional ceramics process has undergone a revolutionary change [23].

3.1.3 Development of ceramic light-curing 3D printing technology

In recent years, there are also more scholars in China who have carried out a lot of work in ceramic light-curing 3D printing. The main research units are Xi'an Jiaotong University, Shenzhen University, Guangdong University of Technology, Beijing Institute of Technology and so on. Xi'an Jiaotong University, such as Li Deduchen belongs to the earlier ceramic SL research team in China, using including oxide ceramic slurry as well as tricalcium phosphate bioceramic slurry, etc. for 3D printing research. A great deal of work has been carried out on the mechanism of ceramic light-curing moulding, the relationship law between ceramic slurry component formulation and light-curing moulding effect, and the application of the process [22,29-34]. Various types of porous or dense ceramic parts, such as porous bone scaffolds, three-dimensional photonic crystals, hollow turbine blades and impeller models, as well as complex structural castings to meet the needs of investment casting, have been manufactured. Due to the low wet strength of water-based ceramic slurry printed parts, most of the ceramic SLs use non-water-based ceramic slurries, which are dominated by acrylate monomer resins. Zhou Weizhao et al [30]investigated in detail the effects of ceramic particle size, solid content, monomer concentration, dispersant, diluent concentration and other factors on the viscosity of ceramic slurry, determined the optimal component content, and successfully developed a new silica-sol-based water-based ceramic slurry, which was prepared with a solids content of up to 50% of the silica-oxide ceramic slurry.Chen et al [37] used this improved water-based environmentally friendly slurry for the printing of SL Chen et al [22]used this improved water-based environmentally friendly paste to conduct an in-depth study on the forming mechanism, the size and precision control of the forming unit and the sintering process, etc., and printed various types of complex structural ceramic parts, and the blanks obtained from printing can maintain good strength and low surface viscosity, which can help in the post-processing process.Bian et al [34]used SL to print tricalcium phosphate cartilage scaffolds with a porous structure in order to obtain good regenerative repair results. In addition, Li Tetsuzumi's team [35]recently used sub-micron zirconia powder slurry to obtain 99.3% densified dental crown and bridge components after DLP light-curing 3D printing and sintering, and the optimised three-stage support design contributed to the smooth printing of the prototype. Some software and hardware optimisation work was also done for the surface exposure process of ceramic DLP to provide technical and theoretical support for improving the print quality [36].

3.2 Intelligent manufacturing technologies applicable to the architectural ceramics industry

Compared to another technology, ceramic SL and DLP process is more suitable for the construction industry. And with the developments of recent years, ceramic SL and DLP processes have proved their worth in the construction industry, offering a degree of design freedom and manufacturing flexibility that is different from traditional construction methods. Both technologies have made it possible to manufacture complex architectural elements and customised components, demonstrating a high degree of efficiency and precision from prototyping through to the production of functionally integrated building blocks. In addition, by breaking through the traditional constraints of design and manufacturing, ceramic SL and DLP technologies are driving the architectural industry in a more personalised and innovative direction. Professionals are now able to explore new design ideas without worrying about the additional costs associated with complexity. And for the restoration and preservation of historic buildings, these technologies offer an effective way to accurately replicate ancient architectural elements, preserving cultural heritage in a non-invasive and sustainable way.

In terms of other technologies, with the development and research of architectural ceramic materials in recent years, considerable achievements have been made, such as the photocatalytic ceramic tiles [37] studied with gC3N4/CuPc composites that can absorb sunlight and decompose hazardous substances (e.g., nitrogen oxides and volatile organic compounds) in the air by photocatalysis, which is a reflection of various technological advances such as green and sustainable technologies, smart ceramic technologies, and surface treatment technologies. The green sustainable technology, smart ceramics technology and surface treatment technology are the embodiment of various technological advances.

4 Existing Problems and Challenges

Since the research and analysis of the China Business Industry Research Institute, although China's building ceramics exports have been on a downward trend since 2015, 2020 by the global epidemic and the impact of the U.S.-China trade friction fall is particularly obvious, 2021, the export volume of the fall slowed down, the downward curve tends to flatten out.2021 China's building ceramics exports of 601 million square metres, a year-on-year decline of 3.40%, the export volume of 4.099 billion U.S. dollars, a year-on-year decline of 0.70%. But with internal and external development advantages and opportunities, China's building ceramics industry in the past decade has been rapid development, has become the world's production and consumption of building ceramics, the world's more than half of the building ceramics produced from China.

In the construction industry, the introduction of modern ceramic materials is seen as an innovation that can provide buildings with increased durability, aesthetics and functionality. Despite the many potential benefits of these materials, their widespread use still faces a number of challenges. Firstly, in practice, modern ceramic materials often require specialised construction techniques. This is not limited to precise installation procedures, but also includes a deep understanding of the material's properties to ensure its correct application. This requires specialised training for the building and construction teams, adding to the complexity and cost of project implementation. In addition, modern ceramic materials are typically higher in cost compared to traditional building materials such as concrete and steel. This adds to the budgetary pressures of construction projects, especially in projects with tighter budgetary constraints, where higher material costs can be an important consideration in material selection. Whilst modern ceramic materials excel in terms of strength, wear resistance and chemical resistance, their brittleness has not been fully addressed. When faced with impact loads or specific harsh environmental conditions, these materials may crack or otherwise suffer damage, which poses a potential risk to the long-term stability and safety of the building. Environmental impact and sustainability issues are also challenges that must be addressed in the development of modern ceramic materials. Although superior to most traditional materials in terms of performance, the high energy consumption and possible environmental pollution of steps such as high-temperature sintering during their production need to be effectively mitigated through technological innovation and process improvement. This is not only about environmental protection, but also the key to public acceptance and market promotion. Finally, modern ceramic materials also need to overcome low market acceptance and poor matching of regulations and standards when promoting their use. It often takes time for the many stakeholders in the construction industry, including designers, engineers, contractors and regulatory bodies, to accept and recognise new materials. In addition, existing building codes and standards may not be fully adapted to the properties of the new materials, requiring continuous communication, testing and adjustment to gradually expand their use in the construction industry.

5 Future Research Directions

According to the literature obtained above. Modern building ceramic materials have gradually become the favourite in the construction industry through their excellent performance, and are gradually entering a steady development trend, while more diversified ceramic matrix composites will become the key direction of development. However, its high cost is still the main factor hindering its wide application. Cost-benefit analyses show that, despite low long-term maintenance costs, high initial investment requirements deter many project owners and developers. This raises an urgent question: how to reduce the cost of these advanced materials through technological innovation and production scale-up so that more projects can benefit. During construction, modern building ceramic materials require a higher level of skill and precision relative to traditional materials, which adds to the complexity and cost of construction. To overcome this challenge, investments need to be focussed on worker training and the development of more efficient installation techniques and tools. For example, the use of digital mouldings and robotic construction techniques has already demonstrated the potential to reduce construction time and improve installation accuracy in some projects. As for environmental and sustainability issues, the production process of modern ceramic materials, despite being more energy efficient and reducing emissions than traditional building materials, still has a certain environmental impact. In the future, further reductions in their environmental footprint are expected through the adoption of circular economy principles, the use of waste materials as raw materials, and the development of lower-energy manufacturing processes. In addition, given the durability and long service life of ceramic materials, their environmental impact may be significantly reduced from a life cycle assessment (LCA) perspective.

6 Conclusion

In summary, in the society aiming at sustainable development, the new type and greening of building materials are the urgent need for sustainable development in the 21st century, and are the main direction for the future development of the construction industry. Ceramic matrix composites are the key direction for the development of modern building ceramic materials. The development and progress of new materials will produce many high-quality, practical, inexpensive building materials, and adhere to the path of sustainable development; maintain the environmental coordination of building materials will also enable the traditional construction industry to play a greater role and characteristics.

Although modern building ceramic materials bring new possibilities to the field of architecture in terms of technology and aesthetics, their wide application still faces challenges such as cost, construction technology, and sustainability. However, the green sustainability technologies and smart ceramics technologies embedded in architectural ceramics motivate us to promote the development and application of these advanced materials, which then require concerted efforts from the industry, academia, and government to address these issues and ultimately lead to more sustainable, cost-effective, and aesthetically pleasing modern building practices.

Acknowledgements: Supported by the Science and Technology Research Program of Chongqing Municipal Education Commission (Grant No.KJQN202204305, and No.KJQN202305501).

References

[1]Luo Y, Wu Y, Ma S, et al.. An eco-friendly and cleaner process for preparing architectural ceramics from coal fly ash: Pre-activation of coal fly ash by a mechanochemical method[J]. Journal of cleaner production, 2019(214):419-428.

[2]Zhang Weiru, Li Ling, Wang Kun. Research status and development trend of advanced ceramic materials[J]. New Material Industry, 2016(1):2-8.

[3]Zhang X, Zhao N, He C. The superior mechanical and physical properties of nanocarbon reinforced bulk composites achieved by architecture design–a review[J]. Progress in Materials Science, 2020(113):100672.

[4]Nie Xianyong, Yao Qingshan, Chen Shulin, et al.. Research and application of digital transformation of building ceramic production line[J]. Foshan Ceramics, 2021,31(11):32-37.

[5]Li K, Yao W, Liu Y, et al.. Wetting and anti-fouling properties of groove-like microstructured surfaces for architectural ceramics[J]. Ceramics International, 2022,48(5):6497-6505.

[6]He Weiwei, Zhao Yun, Le Zhourong. Progress of photocatalytic nano anti-microbial self-cleaning composites[J]. Science and Technology Bulletin, 2023,41(8):113-119.

[7]Xue Zhaolu, Guo Hongbo, Gong Shengkai, et al.. Novel thermal barrier coating ceramic insulation layer material[J]. Journal of Aerospace Materials, 2018(2):10-20.

[8]Zhao N, Mao A, Shao Z, et al.. Anisotropic porous ceramic material with hierarchical architecture for thermal insulation[J]. Bioinspiration & Biomimetics, 2021,17(1):015002.

[9]Yang R, Wang J, An L, et al.. A macromolecular assembly directed ceramic aerogel monolith material[J]. Journal of Materials Chemistry C, 2020,8(30):10319-10324.

[10]Lin Lihan, Wu Xiongzhang. Mechanical aesthetics meets 3D printing: an innovative exploration of interior ceramic decorative design[J]. Foshan Ceramics, 2023,33(11):125-128.

[12]Lu Yumeng. Spatial integration of ceramic product design and architectural interior[J]. Ceramics, 2023 (2):47-49.

[13]Yang Guosong, Ye Chunle. Analysis of the impact of China's construction industry on the environment and suggestions for sustainable development[J]. Sustainable Development, 2020(10):140.

[14]Yang Mengmeng, Wu Yanlong, Chen Xu, et al.. Bio-glass-ceramic bone scaffolds for light-curing 3D printing and degradation[J]. Bulletin of the Chinese Ceramic Society, 2023,42(1):66-69.

[15]Ben Yue, Zhang Le, Wei Shuai, et al.. Research progress of 3D printed ceramic materials[J]. Materials Herald, 2016(21):109-118.

[16]Zhang Wenyu. Research and application of 3D printed ceramic materials[J]. Ceramics, 2020 (6): 40-44.

[17]Heimann, Robert B. Classic and Advanced Ceramics: From Fundamentals to Applications, Preface[D]. John Wiley & Sons, 2010.

[18]Carter, C. B. Norton, M. G. Ceramic materials: Science and engineering[D]. Springer. PP, 2007.

[19]Geiger, Greg. Introduction To Ceramics[J]. American Ceramic Society, 2014(12):66-70.

[20]Chen Zhaofeng, Editor-in-Chief; Li Binbin, et al.. Deputy Editor-in-Chief,Inorganic non-metallic materials (2nd edition)[D]. Northwestern Polytechnical University Press, 2016.

[21]Pei Li zhao. edited,High-tech ceramic materials[D]. Hefei University of Technology Press, 2015.

[22]HULL C W.Methods and apparatus for production of three-dimensional objects by stereolithography: EP0171069A2[P].1986-02-12.

[23]COLOMBO P, MERA G, RIEDEL R, et al.. Polymer-derived ceramics:40 years of research and innovation in advanced ceramics[J]. Journal of the American Ceramic Society, 2010,93(7):1805-1837.

[24]NAKAMOTO T, YAMAGUCHI K.Consideration on the producing of high aspect ratio micro parts using UV sensitive photopolymer[C]. MHS'96 Proceedings of the Seventh International Symposium on Micro Machine and Human Science.Nagoya: IEEE, 1996:53-58.

[25]BERTSCH A, ZISSI S, JEZEQUEL J, et al.. Microstereophotolithography using a liquid crystal display as dynamic mask-generator[J]. Microsystem Technologies, 1997,3(2):42-47.

[26]SUN C, FANG N, WU D, et al.. Projection micro-stereolithography using digital micro-mirror dynamic mask[J]. Sensors and Actuators A:Physical, 2005,121(1):113-120.

[27]HORNBECK L.Digital light processing for high-brightness high-resolution applications[C]. EI'97 Proceedings of SPIE Projection Displays Ⅲ.San Jose: IS & T and SPIE, 1997: 27-41.

[28]ZHANG A, QU X, SOMAN P, et al.. Rapid fabrication of complex 3D extracellular microenvironments by dynamic optical projection stereolithography[J]. Advanced Materials, 2012,24(31):4266-4270.

[29]CHEN Z, LI D, ZHOU W. Process parameters appraisal of fabricating ceramic parts based on stereolithography using the Taguchi method[J]. Proceedings of the Institution of Mechanical Engineers, Part B, 2012,226(7):1249-1258.

[30]ZHOU W Z, LI D C, CHEN Z W, et al.. Curing behaviors of ceramic suspension in stereolithography and its engineering applications[J]. Aeronautical Manufacturing Technology, 2010(8):36-42.

[31]ZHOU W, LI D, CHEN Z, et al.. Direct fabrication of an integral ceramic mould by stereolithography[J]. Proceedings of the Institution of Mechanical Engineers, Part B, 2010, 224(2): 237-243. [32]ZHOU W, LI D, WANG H. A novel aqueous ceramic suspension for ceramic stereolithography[J]. Rapid Prototyping Journal, 2010,16(1):29-35.

[33]BIAN W, LI D, LIAN Q, et al.. Design and fabrication of a novel porous implant with pre-set channels based on ceramic stereolithography for vascular implantation[J]. Biofabrication, 2011,3(3):034103. [34]LIAN Q, WU X, LI D, et al.. Accurate printing of a zirconia molar crown bridge using three-part auxiliary supports and ceramic mask projection stereolithography[J]. Ceramics International, 2019,45(15): 18814-18822.

[35]YANG F, LIAN Q, WU X Q, et al.. Ceramics fabrication using rapid prototyping of mask projection stereolithography[J]. Journal of Mechanical Engineering, 2017,53(7):138-144.

[36]CHEN Z, LI J, LIU C, et al.. Preparation of high solid loading and low viscosity ceramic slurries for photopolymerization-based 3D printing[J]. Ceramics International, 2019,45(9):11549-11557.

[37]YANG Juan, HAO Jingyi, DAI Jun, et al.. Performance and mechanism of mesoporous WO3/H2 O2 photocatalytic oxidation of low concentration gas to methanol[J]. Journal of Coal, 2019,44(10):89-95.

Viser Technology Pte. Ltd.
Research and Application of Materials Science
DOI: 10.33142/rams.v5i2.12709

Research Article Open Access

Preparation and Properties of Bilayer Composite Materials of Cu-coated Fe and CuSn10

Xuan YE [1*], Ling QIN [2], Yuxiang LING [3]

1. Mechanical and Electrical Engineering College, Heyuan Polytechnic, Heyuan, Guangdong, 517000, China
2. R&D Department, Heyuan Peak metal products Co., Ltd., Heyuan, Guangdong, 517000, China
3. R&D Department, Heyuan Yueao Cemented Carbide Co., Ltd., Heyuan, Guangdong, 517000, China

[*] ***Corresponding Author:*** *Xuan YE, E-mail: yexuan1216@sina.com*

Abstract

Bilayer composite materials of Cu-coated Fe and CuSn10 containing 0%, 5%, 10%, 15%, 20%, 25%, 30%, 35%, 40%, 45%, 50% Cu-coated Fe were prepared in mesh belt sintering furnace. Microscopic pore morphology of materials was observed, bending strength was tested. Results show that, There is a good bonding between Cu-coated Fe and CuSn10, with the increase of Cu-coated Fe content from 0% to 50%, bending strength of bilayer composite materials increases.

Keywords: *Cu-coated Fe; CuSn10; bilayer composite*

1 Introduction

Oil-contained bearings are indispensable parts in the machinery industry, which is mainly used in high speed rotating machinery [1-2] and can be prepared by powder metallurgy (PM) technology [3-6]. As the pores exist, which are generated during PM technology, lubricating oil can be stored in PM Oil-contained bearings. Therefore PM Oil-contained bearings have the advantages of low cost and good lubrication performance, etc.

Because of its high content of Cu, which is 10wt%, the cost of CuSn10 alloy PM Oil-contained bearings is relatively higher than Fe alloy PM Oil-contained bearings. And because of its porous loose structure, the strength of CuSn10 alloy PM Oil-contained bearings is relatively lower than Fe alloy PM Oil-contained bearings.

To this end, researchers have developed a Cu-coated Fe composite materials by covering the surface of Fe powder with Cu powder to prepare PM oil-contained bearings[8], in order to improve the strength while further reduce the cost. However, the pore structure of Cu-coated Fe PM oil-contained bearings can not store lubricating oil well, which leads to poor lubrication performance and short service life.

For this purpose, we try to prepare bilayer composite materials containing Cu-coated Fe and CuSn10, in order to synthesize advantages both of high strength, low cost of Cu-coated Fe and good oil storage, lubrication performance of CuSn10, to develop high-performance bilayer composite material of Cu-coated Fe and CuSn10 for oil-contained bearings [9].

In this paper, bilayer composite materials of Cu-coated Fe and CuSn10 containing 0%, 5%, 10%, 15%, 20%, 25%, 30%, 35%, 40%, 45%, 50% Cu-coated Fe were prepared via twice spreading of powder and hydraulic press with pressure of 650 MPa at room temperature, then sintered in mesh belt sintering furnace. Microscopic pore morphology of materials was observed, bending strength was tested.

2 Experiment Method

2.1 Experiment materials

CuSn10 powder and Cu-coated Fe powder were adopted. As shown in Figure 1. Firstly, CuSn10 powder was spread into the mold, then stirred slightly to make it evenly spread to form a layer of CuSn10 powder. Secondly, Cu-coated Fe powder was spread evenly onto the layer of CuSn10 powder. Green compact was prepared via hydraulic press with pressure of 650 MPa at room temperature. Composition proportion is shown at table 1.

Green compact were sintered in mesh belt sintering furnace. The sintering temperature was divided into 6 stages: 816℃ (18 min), 780℃ (18 min), 830℃ (18 min), 830℃ (18 min), 830℃ (18 min), cooling section (90 min), as shown at table 2.

Received on April 23, 2023; Accepted on May 16, 2023

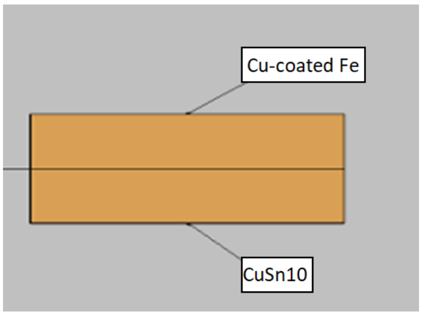

Figure 1 Specimens schematic diagram of bilayer composite materials of Cu-coated Fe and CuSn10

2.2 Performance test

Microscopic pore morphology of sintered samples was observed by metallographic microscope. Three-point bending strength of samples were tested by universal testing machine, size of three point bending specimen is 24.6 mm long, 7.4-9.0mm wide, 8.2-8.6mm high, test span is 18mm.

3 Results and Discussion

3.1 Pore morphology of bilayer composite materials of Cu-coated Fe and CuSn10

Pore morphology of bilayer composite materials of Cu-coated Fe and CuSn10 is shown in figure 2- figure 4. As shown in figure 2(a), 3(a), 4(a), structure of CuSn10 is porous and loose with tiny pores evenly distributed on the matrix, which is a common pore morphology for CuSn10 PM oil-contained bearings. As the pores exist, lubricating oil can be stored to improve the lubrication performance of bearings, but on the other hand, strength of bearings is reduced.

As shown in figure 2(b), 3(b), 4(b), structure of Cu-coated Fe is filled with few and small pores. Obviously, it helps improve the strength of bearings, however, lubricating oil can not be stored, resulting in poor lubrication performance of bearings.

As shown in figure 2(c), 3(c), 4(c), there is a good bonding between Cu-coated Fe and CuSn10. Therefore, bilayer composite materials synthesize advantages both of high strength, low cost of Cu-coated Fe and good oil storage, lubrication performance of CuSn10.

3.2 Bending strength of bilayer composite materials of Cu-coated Fe and CuSn10

Bending strength of bilayer composite materials of Cu-coated Fe and CuSn10 is shown in table 3 and figure 5. As shown at table 3, size of three point bending specimen is 24.6 mm long, 7.4-9.0mm wide, 8.2-8.6mm high, test span is 18mm. As shown in figure 5, bending strength of bilayer composite materials shows increasing trend with the increase of Cu-coated Fe content from 0% to 50%. Especially, Bending strength of bilayer composite materialss containing 30wt% and more Cu-coated Fe are obviously higher than sample#1 prepared by CuSn10 alone. Moreover, bilayer composite materials containing 50wt% Cu-coated Fe have the highest bending strength of 432.65MPa, which is 18.66% higher than pure CuSn10 material.

Table 1 Specimens composition proportion (wt %)

Sample Number	Cu-Sn10 (g)	Cu-Fe (g)	Cu-coated Fe content (wt%)
	12	0	0%
	11.4	0.6	5%
	10.8	1.2	10%
	10.2	1.8	15%
	9.6	2.4	20%
	9.0	3.0	25%
	8.4	3.6	30%
	7.8	4.2	35%
	7.2	4.8	40%
	6.6	5.4	45%
	6.0	6.0	50%

Table 2 Sintering process of specimens

Sintering stage	Temperature /℃	Time/min
	816	18
	780	18
	830	18
	830	18
	830	18
	cooling section	90

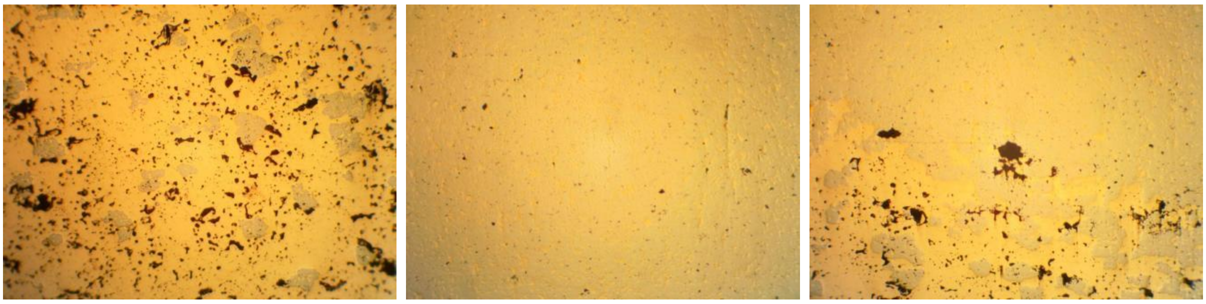

(a)Pure CuSn10 region (100X) (b)Cu-coated Fe region (100X) (c)interface bonding region (100X)

Figure 2 Pore morphology of bilayer composite materials of 5wt% Cu-coated Fe and CuSn10

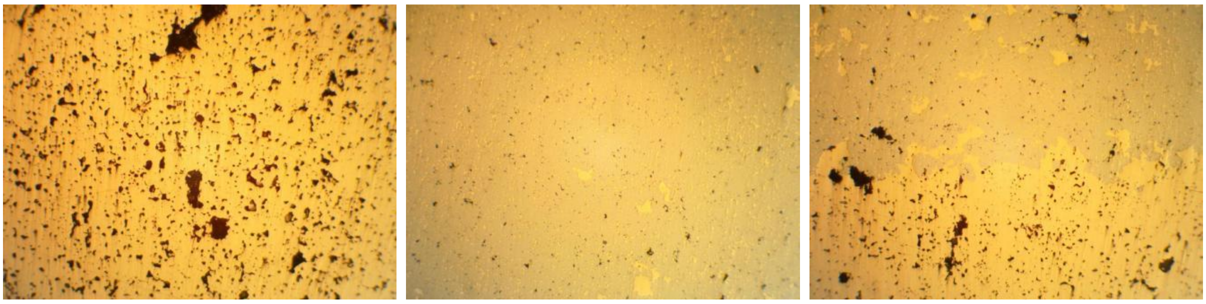

(a)Pure CuSn10 region (100X) (b)Cu-coated Fe region (100X) (c)interface bonding region (100X)

Figure 3 Pore morphology of bilayer composite materials of 35wt% Cu-coated Fe and CuSn10

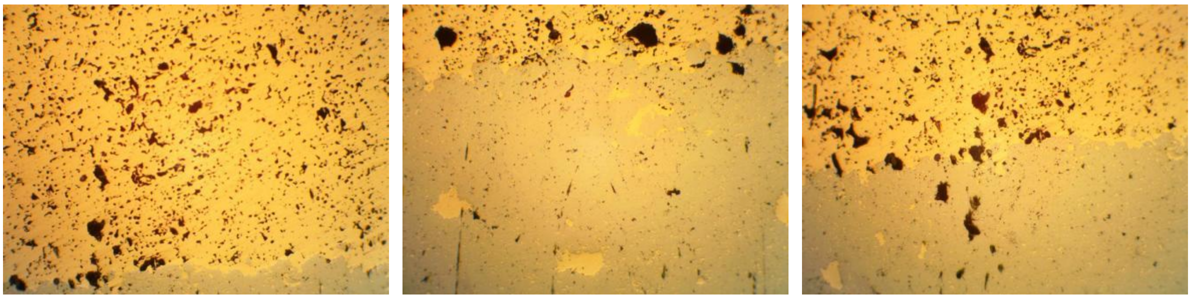

(a)Pure CuSn10 region (100X) (b)Cu-coated Fe region (100X) (c)interface bonding region (100X)

Figure 4 Pore morphology of bilayer composite materials of 50wt% Cu-coated Fe and CuSn10

Table 3 Bending strength of bilayer composite materials of Cu-coated Fe and CuSn10

Sample Number	CuSn10 (wt%)	F （N）	L (test span mm)	b (width mm)	h (height mm)	Bending strength (MPa)
	0%	7721	18	8.4	8.3	364.61
	5%	6477	18	8.5	8.3	298.65
	10%	8472	18	8.4	8.3	395.29
	15%	7500	18	8.5	8.3	345.82
	20%	6363	18	7.4	8.3	334.48
	25%	7784	18	8.9	8.6	319.29
	30%	9049	18	8.7	8.2	420.67
	35%	9564	18	9.0	8.2	422.58
	40%	9467	18	8.7	8.3	427.46
	45%	9367	18	8.9	8.2	421.67
	50%	9604	18	8.7	8.3	432.65

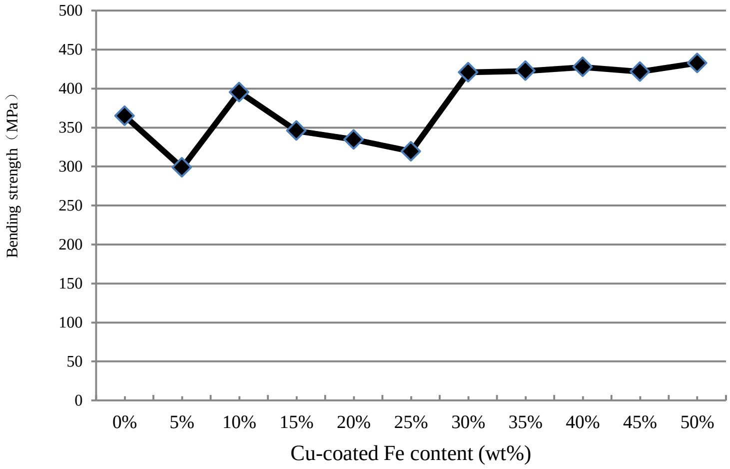

Figure 5 Bending strength of bilayer composite

4 Conclusion

Bilayer composite materials of Cu-coated Fe and CuSn10 with good interface bonding can be prepared via twice spreading of powder and hydraulic press at room temperature, which can synthesize advantages both of high strength, low cost of Cu-coated Fe and good oil storage, lubrication performance of CuSn10. (2) Bilayer composite materials containing 30wt% and more Cu-coated Fe show better mechanical properties, of which, materials containing 50wt% Cu-coated Fe have the highest bending strength of 432.65MPa, which is 18.66% higher than pure CuSn10 material.

Fund Project: Research project of Heyuan polytechnic(2022ky05, 2022ky06); 2019 Provincial Science and Technology Special Fund (" Big project "+" Task List ") project(2019005, 2019004).

References

[1]LI Dongyu, LI Xiaoqiang, LI Jingmao, et al.. Effect of Sintering Process on Microstructure and Properties of Copper-Iron-based Oil-impregnated Bearing[J]. Materials Reports, 2021,35(8):8157-8163.

[2]HUANG Zhao-xuan, LAN Jiang, YANG Shi-yu, et al.. Effect of MoS_2 and graphite on friction properties of bronze oil bearing[J]. Powder Metallurgy Technology, 2020,38(5):363-370.

[3]YE Xuan, TU Huajin, QIN Ling, et al.. Properties of Fe-Cu-C composite reinforced by different WC content[J]. IOP Conference Series: Materials Science and Engineering, 2019, 688(3):109-112.

[4]YE Xuan, QIN Ling. Preparation and performance of WC/TiC reinforced iron matrix composites[J]. Powder Metallurgy Industry, 2021,31(4):49-54.

[5]YE Xuan, TU Huajin, QIU Zhiwen, et al.. Effects of WC Content on Pore Morphology and Properties of Fe-1.5Cu-1.8Ni-0.5Mo-1C PM Composite[J]. Hot Working Technology, 2019,48(22): 89-93.

[6]YE Xuan, TU Huajin, QIU Zhiwen, et al.. Effect of WC particle reinforcement on Fe–1.5Cu–1.8Ni–0.5Mo–1C P/M composite[J]. Powder Metallurgy Technology, 2019,37(1):40-45.

[7]WANG Jingxuan, WANG Jiaqi, YIN Yanguo, et al.. Dry Friction Characteristics of FeS/Cu-Bi Copper-Based Sliding Bearing Materials[J]. Bearing, 2020(3):39-43.

[8]ZHANG Shanshan, LI Changyun, PAN Yuewu, et al.. Application and preparation of copper-coated iron powders[J]. Powder Metallurgy Technology, 2020,38(6):465-474.

[9]Yang Lei, Gao Qiu, Liu Hong, et al.. Fabrication and Properties of Dual-Gradient Nanostructured Copper Matrix Composites Reinforced by Silicon Carbide Particles[J]. Powder Metallurgy Technology, 2016,34(6):428-433.

Publisher: Viser Technology Pte. Ltd.

URL: www.viserdata.com

Add.:21 Woodlands Close, #08-18,

Primz Bizhub SINGAPORE (737854)

ISSN 2661-4456